

A novel friction weakening-based dynamic model for landslide runout assessment along the Sichuan-Tibet Railway



Jian Guo^a, Yifei Cui^{a,*}, Wenjie Xu^a, Wei Shen^{b,c}, Tonglu Li^{b,c}, Shujian Yi^{d,e}

^a State Key Laboratory of Hydroscience and Engineering, Tsinghua University, Beijing 100084, China

^b Department of Geological Engineering, Chang'an University, Xi'an 710064, China

^c Water Cycle and Geological Environment Observation and Research Station for the Chinese Loess Plateau, Ministry of Education, Zhengning 745399, China

^d Key Laboratory of Mountain Surface Process and Hazards/Institute of Mountain Hazards and Environment, Chinese Academy of Sciences, Chengdu 610041, China

^e University of Chinese Academy of Sciences, Beijing 100049, China

ARTICLE INFO

Keywords:

Numerical simulation
Friction weakening
Lagang ancient landslide
Risk assessment
Sichuan-Tibet Railway

ABSTRACT

The Sichuan-Tibet Railway traverses the Qinghai-Tibet Plateau in China, where giant landslides occur frequently and densely. Accurately assessing the velocity, runout distance, and influenced area of the potential landslides is one of the nonnegligible scientific and technical issues. This study establishes a dynamic model for the landslide runout assessment along the Sichuan-Tibet Railway. The proposed model is based on the shallow water theory and takes into account the mechanism that the friction is weakening with the increase of velocity, the finite difference method is used to solve the governing equations, and the ideal one-dimensional dam break experiment was used to verify the shock-capturing capacity of the numerical methods. The Lagang ancient landslide, only 500 m away from the Jiacha Station of the Sichuan-Tibet Railway, represents the typical environment and development pattern of landslides in this region. Therefore, the proposed model is applied to discuss its effects on the landslide dynamic process and deposit patterns. Besides, 75 sets of numerical experiments were further carried out to explore the sensibility of the three parameters including peak friction coefficient μ_p , steady friction coefficient μ_s , and critical velocity V_c in this model. The results indicate that μ_s determine the lower limit of the friction coefficient, which significantly impacts the landslide runout distance; μ_p is mainly acting at the initial and final stage and has less influence on the landslide dynamic. By contrast, V_c is the most significant. When the V_c is small, the landslide can quickly reach the threshold velocity after the initial, and the dynamic process has a small correlation with the μ_p ; when the V_c is large, the landslide is difficult to reach the threshold, and the mobility will be limited. It should be noted that the materials, lithology, strength, and micro-cracks of landslides mass formed under the special geological, geomorphic, and climatic conditions in this region may affect the input values when using the friction weakening model on landslides risk assessment.

1. Introduction

The Sichuan-Tibet Railway passes through the Qinghai-Tibet Plateau, which is famous for its complex geological, topographic, tectonic, and climate change (Cheng and Wu, 2007; Pan et al., 2012; Xue et al., 2021). Because of the active tectonic movement, dense active faults, high seismic intensity, and significant topographical changes, there has become a hotbed of natural hazards (Cui et al., 2010; Cui and Jia, 2015; Wei et al., 2020; Yan et al., 2021; Zhang et al., 2021a). The Sichuan-Tibet Railway is exposed to the complex topography and always faces the threat of high-velocity and long-runout landslides (Dai et al., 2019; Zhou et al., 2016). Catastrophes disaster chains of “landslide-

debris flow-dam lake-outburst flood” were then always formed (Cui and Guo, 2021), which has become a major challenge for the selection, construction, and operation of the Sichuan-Tibet Railway (Cui et al., 2021; Peng et al., 2020).

The high-velocity and long-runout landslides along the Sichuan-Tibet Railway is significantly shaping and changed the regional geomorphology since ancient times (Li et al., 2020b; Qi et al., 2021; Zhou et al., 2021). In 2000, a huge landslide occurred in Yigong with a volume of more than 3×10^8 m³. The traffic facilities along Palong Tsangpo and the Yarlung Zangbo River were destroyed by the dammed lake and outburst flood (Li et al., 2020a). Some landslides in this region can even be traced back to the tectonic period. For instance, the Luanshibao

* Corresponding author.

E-mail address: yifeicui@mail.tsinghua.edu.cn (Y. Cui).

landslide occurred 3700 years ago with about $4 \times 10^7 \text{ m}^3$ of the deposits (Wang et al., 2018; Zeng et al., 2020). As a region where the Sichuan-Tibet Railway passed, the stability of landslide deposits and the risk of recurrence are issues that must face (Yan et al., 2021). In addition, some ancient landslides in this region were even overlooked for their insignificant characteristics. In Basu County, a newly discovered landslide with a volume of $35 \times 10^8 \text{ m}^3$, almost 4.6 times the Daguangbao landslide, which might be the largest one in China (Cui et al., 2018; Deng et al., 2021; Yin et al., 2011).

Carrying out the risk assessment of the high-velocity and long-runout landslides along the Sichuan-Tibet Railway is of great significance to its design, construction, and operation. The dynamic process of the landslide is usually reconstructed by various numerical simulation methods including MPM, SPH, DEM, DDA, and other methods (Fan et al., 2019a; Liu et al., 2020; Yan et al., 2020; Zou et al., 2017). Although, each of them is based on different physical mechanisms and considers different factors in the movement of the landslide (Kang and Chan, 2018), most of which are still in the stage of theoretical research (see Table 1). Limited by the calculation efficiency, they have not been widely used in landslides risk assessment. Contrastly, the Shallow Equation Method (SEM) is relatively mature with an efficient numerical solution format (Kang and Chan, 2018). It has been used and verified in plenty of cases, and has developed as one of the best choices as a framework for landslide runout analysis (Guo et al., 2020; Sassa et al., 2010).

Resistance characteristics are one of the most important factors affecting the dynamic process of geophysical mass flow (Borykov et al., 2019; Wang and Sassa, 2010). The resistance model in the traditional study was usually based on a constant global static resistance coefficient, which was suitable for landslides with large volumes and small runout distances (Fan et al., 2019a; Ouyang et al., 2017). However, it is different in high-velocity and long-runout landslides due to the complex interaction between the above mass and the based bed (Goren and Aharonov, 2007; Kang and Chan, 2018). The resistance of the landslide during the starting, acceleration, deceleration, and deposition stage may vary greatly with velocity (Lucas et al., 2014; Togo et al., 2014). The geomechanics of friction weakening has been developed by plenty of hypotheses such as flash heating mechanism, liquefaction mechanism, dynamic crushing mechanism, bottom entrainment mechanism, shear vibration mechanism, and momentum transfer mechanism (Diao and Espinosa-Marzal, 2018; Hu et al., 2020; Kuwano and Hatano, 2011; Togo et al., 2014). Both laboratory and numerical studies have indicated that using a static resistance coefficient for risk assessment may underestimate the results.

To take into consideration the influence of the various resistance in numerical simulation, Shen et al. (2018) adjusted the friction coefficients in different regions by experience, which requires adjustment of parameters based on the area of the actual deposits and it is suitable for back analysis based on detailed field date (Fan et al., 2019a; Schaub

et al., 2015). For the landslide risk assessment, it needs to assess the influenced range or even the dynamics process before the landslide (Dai et al., 2002; Ouyang et al., 2019), so the empirical method shows great limitations. On the one hand, it has high requirements for on-site data, which violates the intentions of risk assessment on a large scale; on the other hand, the empirical value has strong subjectivity and lacks the need actual accumulation range for calibration, which may lead to errors in the assessment results.

Accurately predicting the time, sites, and dynamic process of the potential landslides is still a challenge because most of the dynamic models need back analysis (An et al., 2021; Ouyang et al., 2017). Therefore, a positive evaluation method based on physical mechanisms needs to be proposed (Cui and Guo, 2021). In these years, the research on friction weakening is mainly based on experimental with micro-scale (Yang et al., 2014). Some of the numerical studies have always applied these conclusions, in which the input parameters are also based on these studies (Liu et al., 2015). Limited by the experimental settings, the threshold parameters obtained may be different from the actual dynamic process. Therefore, the simulation results may not truly reflect the dynamic process and influenced region when carried out the landslide risk assessment. Unfortunately, less attention has been paid to the previous research. For the above reasons, an urgent need is raised to develop a landslide dynamic model that considers the friction weakening mechanism and uses it in landslides assessment along the Sichuan-Tibet Railway.

In this study, a landslide dynamic model based on the two-dimensional depth-integrated model was proposed based on the basic framework of Shen et al. (2018) by further considering the friction weakening mechanism developed by Lucas et al. (2014). Then, the numerical accuracy was tested by an ideal two-dimensional dam-break experiment. The Lagang ancient landslide, which is 500 m away from the Sichuan-Tibet railway, is selected as the typical case to further discuss the parameter sensitivity of the speed-based resistance weakening model. At the end of the paper, we further discussed the geophysical meanings of the model parameters and their influences on the landslide dynamic process. This study could provide tools and theoretical support for the high-speed and long-runout landslide risk assessment along the Sichuan-Tibet Railway.

2. Methodology

Due to the long moving distance of the landslide, the sliding mass is usually sufficiently disintegrated, and it can be simplified as a flow of debris mass (Pudasaini and Krautblatter, 2014; Zhang and McSaveney, 2017). In these kinds of landslides, the influenced range in the horizontal direction is usually much larger than the thickness, which satisfies the assumptions of the shallow water equations with a depth average method. Therefore, shallow water equations based on fluid

Table 1
Mechanisms and characters of different numerical methods for landslides risk assessment.

Method	Mechanism	Advantage	Disadvantage	Reference
Material Point Method (MPM)	Coupled Lagrangian particles and Eulerian background grid to solve internal state variables	Can avoid grid distortion, suitable for large deformation and fracture simulation	Low calculation efficiency	Sulsky et al. (1994)
Smoothed Particle Hydrodynamics (SPH)	Solve the dynamic equations of the particle group, track the mass, velocity, and movement of each particle, and obtain the behavior of the system	Meshless method, low requirements for particle arrangement, suitable for large deformation simulation	Complicated modeling process, large calculation amount, and low calculation efficiency	Crespo et al. (2015)
Distinct Element Method (DEM)	The contact between discrete elements produces deformation and displacement, which in turn produces movement	Simple contact detection laws and clear physical mechanism	Complex contact models, large calculation amount, and low calculation efficiency	Cundall and Strack (1979)
Discontinuous Deformation Analysis (DDA)	Establish a balance equation based on the principle of minimum potential energy, solve the displacement and deformation at the same time	Has advantages in simulating rock mass structural	Complicated contact detection laws, large calculation amount, and low calculation efficiency	Shi and Goodman (2010)
Shallow Equation Method (SEM)	Solving two-dimensional shallow water equation based on depth integral theory	Relatively mature with high calculation efficiency, widely used in hazards risk assessment	Missing information such as internal collisions	Savage and Hutter (1989)

mechanics are used to describe their dynamic process. The governing equations of both mass and momentum conservation were deduced from a rectangular soil column, which is the basic element of the landslide mass (Sassa et al., 2010; Shen et al., 2018).

2.1. Governing equations

In this model, the sliding mass is simplified as a series of soil columns, each of which is subjected to lateral earth pressure P , gravity W , resistance S , and supporting force N (as shown in Fig. 1). The sliding mass moves with mass and momentum exchange between the adjacent grids. Therefore, the governing equations include both mass and momentum conservation in the X and Y directions.

In this model, the mass conservation equation in rectangular Cartesian coordinates with vertical z-axis can be derived as:

$$\frac{\partial h}{\partial t} + \frac{\partial Q_x}{\partial x} + \frac{\partial Q_y}{\partial y} = 0 \quad (1)$$

where h represents the flow depth of the sliding mass; t is the time; i is the direction (X and Y), Q_i and v_i are the velocity and net flow flux of landslide material in two directions, respectively, which can express as:

$$Q_i = v_i h \quad (2)$$

The momentum conservation equations in rectangular Cartesian coordinates with vertical z-axis can be derived as:

$$\frac{\partial Q_x}{\partial t} + \frac{\partial Q_x^2/h}{\partial x} + \frac{\partial Q_x Q_y/h}{\partial y} = - \left(k_x g h \frac{\partial h}{\partial x} + \frac{g h^2}{2} \frac{\partial k_x}{\partial x} \right) + (A g + B) \frac{h \tan \alpha}{G} - D_x S \quad (3)$$

$$\frac{\partial Q_y}{\partial t} + \frac{\partial Q_y^2/h}{\partial y} + \frac{\partial Q_x Q_y/h}{\partial x} = - \left(k_y g h \frac{\partial h}{\partial y} + \frac{g h^2}{2} \frac{\partial k_y}{\partial y} \right) + (A g + B) \frac{h \tan \beta}{G} - D_y S \quad (4)$$

Where k_i is the lateral earth pressure coefficient in the X and Y direction; $g = 9.8 \text{ m/s}^2$ is the gravity acceleration; α and β are terrain angles in the X and Y directions, respectively ($\tan \alpha = \partial Z / \partial x$, and $\tan \beta = \partial Z / \partial y$, in which Z is the bed elevation); S and D_i are the resistance force and their direction. Both A , B , and G are the intermediate parameters. Among them, A and B are static force and centrifugal force, G is a term related to terrain. Following Shen et al. (2019a), they could be expressed as follows:

$$D_i = \frac{v_i}{\sqrt{v_x^2 + v_y^2}} \quad (i = x, y) \quad (5)$$

$$A = 1 + k \frac{\partial h}{\partial x} \tan \alpha + k \frac{\partial h}{\partial y} \tan \beta \quad (6)$$

$$B = \frac{C_x}{\cos \alpha} \left(\frac{v_x}{\cos \alpha} \right)^2 + \frac{C_y}{\cos \beta} \left(\frac{v_y}{\cos \beta} \right)^2 \quad (7)$$

$$G = \tan^2 \alpha + \tan^2 \beta + 1 \quad (8)$$

where C_x and C_y are the topographic curvatures.

The lateral earth pressure of the sliding mass includes active, passive, and static earth pressure, and following the suggestion of Savage and Hutter (1989), the lateral pressure coefficient k can be expressed as:

$$k = \frac{2}{\cos^2 \phi} \times \left[1 \pm \sqrt{1 - (1 + \mu^2) \cos^2 \phi} \right] - 1 \quad (9)$$

Where ϕ is the internal friction angle and μ is the bottom friction coefficient of the sliding mass, “-” and “+” represent the active or passive state, respectively. The sliding mass is spreading when $\partial u / \partial x + \partial v / \partial y \geq 0$ and compressing when $\partial u / \partial x + \partial v / \partial y < 0$.

In the previous study, different resistance models such as the Bingham model, Voellmy model, and Mohr-Coulomb model were used to represent the different kinds of sliding mass (Iverson, 2012; Kang and Chan, 2018; Mikoš and Bezak, 2021; Ouyang et al., 2019; Shen et al., 2019b). These years, a velocity-based friction weakening model has been proposed and developed based on statistics of a large number of high-velocity and long-runout landslides (Lucas et al., 2014; MiDi, 2004). In this model, the friction coefficient μ of a high-velocity and long-runout landslide correlates with its velocity, which can be expressed as:

$$\mu = \mu_s + (\mu_p - \mu_s) e^{-V/V_c} \quad (10)$$

where μ_s is defined as the steady frictional coefficient, μ_p is the peak friction coefficient, and V_c is a material constant that represents the threshold velocity.

In this study, the friction weakening model as introduced before was used to replace the resistance models based on Lucas et al. (2014), by which the friction term in this model can be expressed as:

$$S = g h (\mu_s + (\mu_p - \mu_s) e^{-V/V_c}) \quad (11)$$

2.2. Model setup and numerical scheme

The numerical scheme of this model has been detailed and introduced by Shen et al. (2018). Each soil column element will be static before the initial. They will accelerate and starts moving when the driving force (such as lateral pressure and gravity) is greater than the resistance. So the initial condition can be expressed as:

$$\left| (A g + B) \frac{h \tan \alpha}{G} - \left(k_x g h \frac{\partial h}{\partial x} + \frac{g h^2}{2} \frac{\partial k_x}{\partial x} \right) \right| > |D_x S| \quad (12)$$

The termination conditions of the model include two situations. In

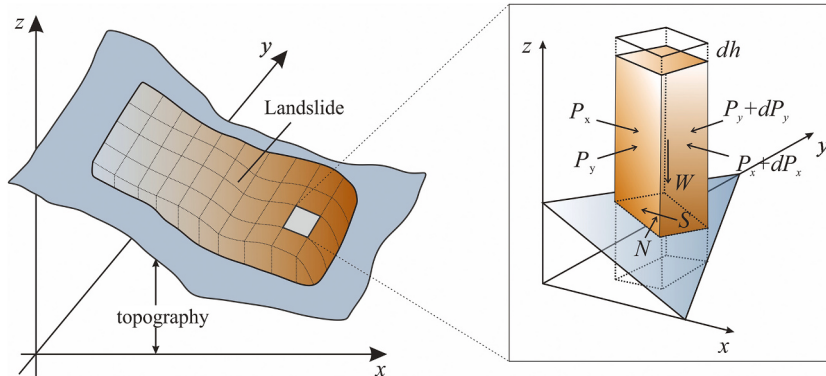


Fig. 1. Schematic diagram of the landslide dynamic model and force analysis of the basic soil column element.

the first situation when a specific calculation time (or steps) was set, the simulation stops when beyond this value. In another case, the simulation will end if the average velocity is less than 0.1 m/s when the above value was null Shen et al. (2021).

The simulation domain should be large enough to ensure the landslide mass will not be running out of its boundary. Following Ouyang et al. (2013), a variable computational domain is used in simulation, and its boundary refers to the meshes between landslide mass covering ($h > 0$) and without covering ($h = 0$). This region varies in each step. The velocity of the boundary element is set to zero at the beginning. Similar to other depth integral models, the free surface boundary is automatically determined based on the thickness of sliding mass (Frank et al., 2015; Hussin et al., 2012).

2.3. Verification

The ideal one-dimensional dam break experiment was widely used to verify the shock-capturing capacity of the numerical methods. In this test, the ground is level and frictionless. When the dam suddenly breaks, the water starts to move without considering the entrainment. The analytical solution of the whole process has been proposed and verified by Stoker and Lindsay (1958), which has also been used to verify the numerical model by scholars (Liang et al., 2006; Ouyang et al., 2013; Zoppou and Roberts, 2000). Similar to these studies, the initial upstream water depth in this study is set to 1.0 m, and the initial downstream water depth is set to 10^{-1} m, 10^{-3} m, and 10^{-6} m, respectively. In addition, the gravity acceleration is set to $g = 9.8 \text{ m/s}^2$, and the density of the mass is set as 1000 kg/m^3 , which is the same as the initial condition of Ouyang et al. (2013). Fig. 2 shows the distribution of the height and velocity of the water wave under three different water depths at $t = 0.1 \text{ s}$. The numerical simulation results were used to compare with the analytical solutions (Stoker and Lindsay, 1958) and the results of the MacCormack-TVD format by Ouyang et al. (2013). The results suggest that our model has a good shock-capturing capacity, which also indicates the good robustness of the proposed model.

3. Case study

3.1. The Lagang ancient landslide

The Lagang ancient landslide is located in the west of Jiacha County,

Shannan Region in Tibet (Fig. 3a). It belongs to the middle reaches of the Yarlung Zangbo River in the south-central Qinghai-Tibet Plateau. The Jiacha Station, one of the important transportation hubs of the Sichuan-Tibet Railway, is only 500 m away from the Lagang ancient landslide. The main sliding direction of the Lagang ancient landslide is 183° from north to south, and it shows a “tongue” shape in planar view (Fig. 3b). The sliding direction of the landslide is perpendicular to the extension of the Yarlung Zangbo fault, which passed the waist of the slope. The landslide scar is located in the north with an elevation of 4215 m, and the toe of the slope is in the south with an elevation of 3320 m. The Yarlung Zangbo River flow is in front of the landslide deposits. The maximum horizontal and vertical runout distance of the landslide is 3000 m and 965 m, respectively (Fig. 4). Therefore, the average gradient of the landslide is 18° . The instability area at the trailing edge has a steeper slope of 31° , and the movement and accumulation areas are relatively gentle at 7° , which is located on the terrace of the Yarlung Zangbo River. The landslide covers an area of 1.16 km^2 , and its volume is estimated to be about $3.23 \times 10^7 \text{ m}^3$.

The cross-section map of the Lagang ancient landslide was shown in Fig. 4 based on the field investigation and takes a reference to Wu et al. (2018). The back scar of the landslide is dominated by a thick conglomerate with an occurrence of $176^\circ \angle 35^\circ$. The sliding surface was flat and smooth although it has weathered for nearly 4867 ± 513 – 8710 ± 963 years based on ^{10}Be age tests from Wu et al. (2018). The area of the source area is $48 \times 10^4 \text{ m}^2$, and the average thickness is 80 m. The shearing crack is located at the bottom of the sliding surface where a suture belt passes (Fig. 5a). The suture zone cuts the mountains on the north side of the Yarlung Zangbo River, forming a series of fault triangles. The deposition area is located on the terrace of the Yarlung Zangbo River, and the bottom of the terrace is feldspar quartz sandstone. The deposition area presents a significant form of high-velocity and long run-out landslide, and the giant conglomerate rocks from the source area are widely distributed near the Lagang Village, 1500 m away from the instability area, with a maximum diameter of even more than 40 m (Fig. 5c, d). These phenomena suggest the super mobility of the landslide. It is found that the accumulation mass on the left bank of the Yarlung Zangbo River is high and steep, at least 20 to 30 m above the water surface, and the river channel was severely cut. No giant conglomerate was found in the river channel and on the opposite bank. Therefore, it can be preliminarily judged that the Lagang ancient landslide once moved into the river course, and then formed the current

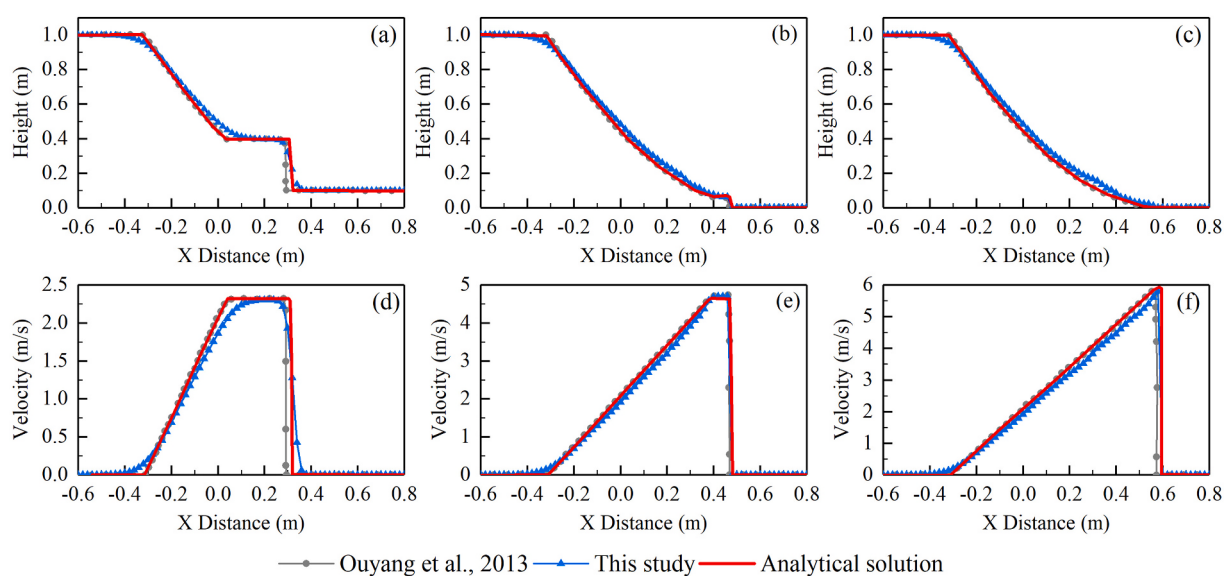


Fig. 2. Comparison of the analytical and numerical solutions of dam failure with different downstream water depths (10^{-1} m for Fig. 2(a) and 2(d), 10^{-3} m for Fig. 2(b) and 2(e), 10^{-6} m for Fig. 2(c) and 2(f)).

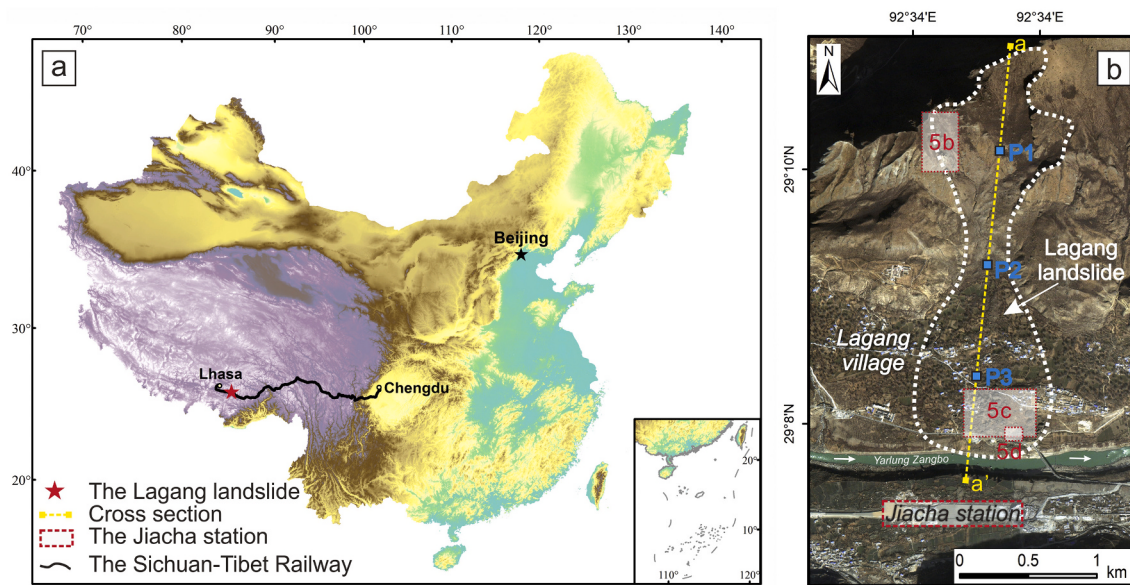


Fig. 3. The location of the Lagang ancient landslide on the Qinghai-Tibet Plateau. (a) the study area and its location in the Sichuan-Tibet Railway; (b) general view of the Lagang ancient landslide (from Google Earth, Date: 2010/03/21).

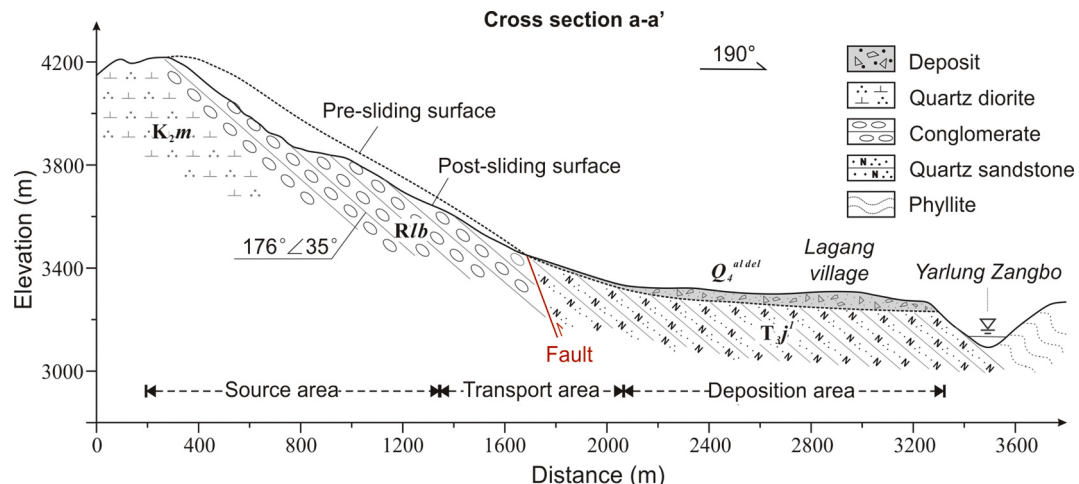


Fig. 4. Geological section (a-a' in Fig. 3b) of the Lagang ancient landslide in Jiacha County (Based on Wu et al. (2018)).

landform under the action of river erosion.

The Lagang ancient landslide represents one of the most typical modes of the long-runout landslide along the Sichuan-Tibet Railway, especially in the Jiacha-Langxian section. Understanding the formation mechanism and dynamic process of the Lagang ancient landslide will provide a significant reference for future landslide prevention along the Sichuan-Tibet Railway. As mentioned above, the Lagang ancient landslide may occur 4000 to 10,000 years ago during the Interglacial period with significant glacier melting (Bazai et al., 2021; Dergachev, 2015; Wu et al., 2018). The scar of the Lagang ancient landslide is near the snow line with an average altitude of 4200 m on the top of the mountain. The freezing and thawing effect is so strong to reduces the integrity and strength of the rock mass. At the same time, the Yarlung Zangbo River fault, with strong mobility, is located at the waist of the Lagang ancient landslide (Fig. 5a), which provides a perfect cut-out position for the instability. The on-site investigation indicates that the source area was perfectly located between the top of the mountain and the fault zone, which confirmed the above conjecture. It has been widely accepted that landslides, especially large-scale landslides, are usually induced by earthquakes which may transfer huge energy to the rocks (Fan et al.,

2019b; Li et al., 2021b). Field investigation shows that the thickness of the rupture mass is close to 80 m (Fig. 5b). Therefore, it's hard to doubt that the Lagang ancient landslide is not the masterpiece of the earthquake. The projectile hypothesis has been put forward to explain this phenomenon and applied in the Dagangbao landslide (Zhu et al., 2020), and Luanshibao avalanche (Wang et al., 2018). The nonlinear distribution of the deposits where giant gravels with a diameter of 10–40 m, are mainly concentrated near Lagang Village far away from the source area rather than near the foot of the slope, confirms the above point of view to a certain extent (Fig. 5c).

3.2. Simulation setup

The terrain used in the simulation was derived from aerial photos of drones (by DJ Mavic 2 pro). The obtained unmanned aerial system (UAS) imagery was processed using the Agisoft PhotoScan, a commercial software extensively used in the UAS community. The photogrammetric workflow finally provides a DSM resolution of 5 cm and altitude uncertainties of ± 3 cm, which allows the scaring mark detection in the corresponding differential DSM. The terrain before sliding, they were

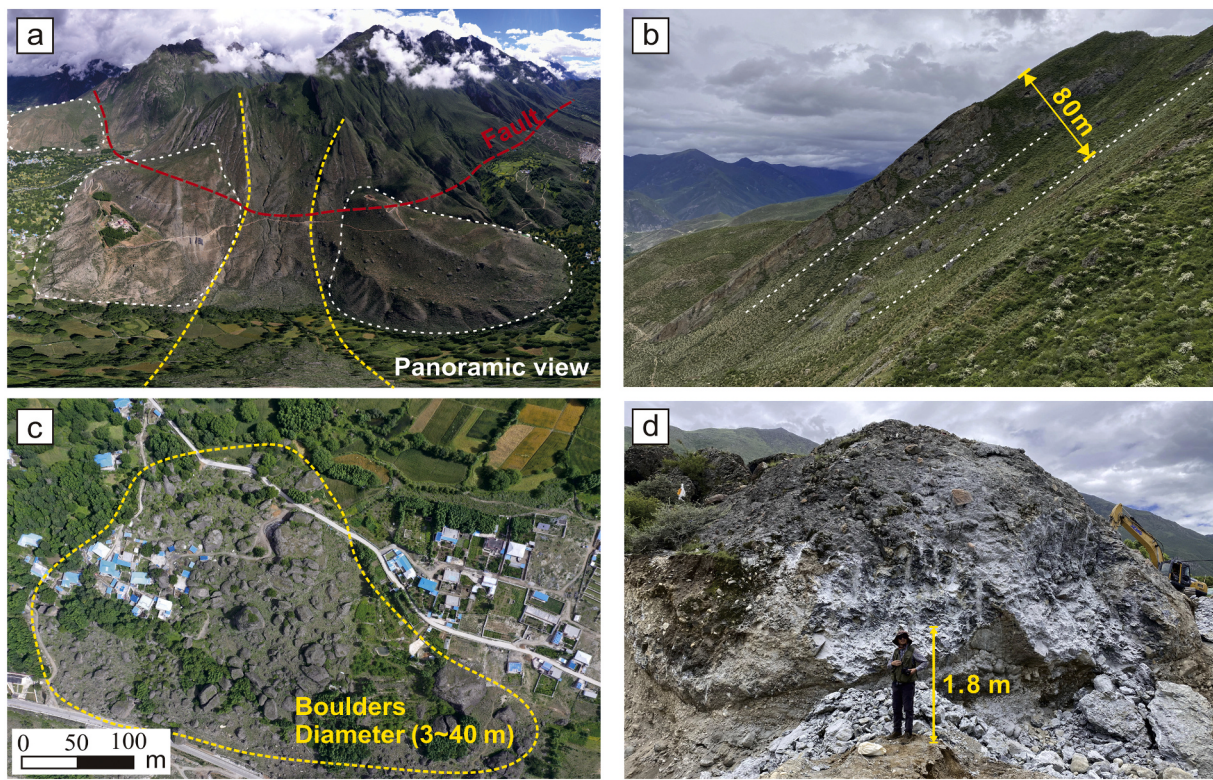


Fig. 5. The details of the Lagang ancient landslide (a) Panoramic view of the landslide source and transport area, with a fracture passing through the shear crack; (b) The huge control joint surface on the right side of the landslide back edge; (c) Giant conglomerate widely distributed in the accumulation area; (d) Typical conglomerate rock block.

reconstructed according to the rock formation and slope terrain based on the acquired contour line since the landslide occurred thousands of years ago, the above operations are carried out in ArcGIS software. To ensure the accuracy and efficiency of the calculation, the computational grids in this study are 798×441 (351,918 in total), and the size of each grid is 5×5 m.

Two serious simulations have been carried out in this study. To begin with, a series of fixed friction coefficients ($\mu = 0.3, 0.35, 0.4, 0.45, 0.5, 0.55, 0.6$) were applied to study its effect on the depositions. Then, the friction weakening model is considered, we systematically reviewed the values of the friction weakening model in the previous study as shown in Table 2. It is noticed that the ranges of μ_p , μ_s , and V_c vary greatly in different situations. The value of μ_p ranges between 0.6 and 0.8, and the value of μ_s ranges between 0.1 and 0.3. In contrast, the range of V_c varies greatly. For the Rotary-shear tests, it is usually around 0.1 m/s, and for the numerical simulation, it is mainly around 4 m/s. The difference may be related to the materials (such as clay and quartz minerals). Besides, the acquisition method may also affect the weakening threshold, because the shearing speed in the laboratory is difficult to reach tens of meters per second, however, they are very common in large landslides. Fig. 6 shows the statistics of the relationship between the volume of the landslide and the effective friction coefficient on the earth (Lucas et al., 2014). It is found that the Lagang ancient landslide is in good agreement with the fitted curve (Fig. 6). To explore the influence of the resistance weakening model on landslide dynamics, 75 sets of numerical tests were further carried out with a relatively large initial range referring to the actual cases and experiments (Table 2). The detailed variables for the numerical tests were shown in Table 3.

The physical parameter that needs to be input into the model is the density ρ of the sliding mass, and it was calculated by dividing the weight and volume of the cylinder samples by standard volume ($D_s = 5$ cm, $H_s = 10$ cm). In addition, the peak friction coefficient μ_p , the steady friction coefficient μ_s , and the critical velocity V_c should be input before

Table 2

Different parameters values of the friction weakening model used in the previous study.

μ_p	μ_s	V_c (m/s)	Materials	Methods	Reference
0.7	0.162	0.1	Dry powders, fault gouges	Rotary-shear test	Togo et al. (2014)
0.61	0.098	0.11	Wet shale powders	Rotary-shear test	Miyamoto et al. (2009)
0.22	0.081	0.1	Wet fault gouges	Rotary-shear test	Miyamoto et al. (2009)
0.38	0.076	0.15	Semi-wet fault gouges	Rotary-shear test	Yang et al. (2014)
0.63	0.18	1.03	Nojima fault gouge	Rotary-shear test	Mizoguchi et al. (2007)
0.61	0.093	0.198	Shale powder	Rotary-shear test	Dong et al. (2013)
0.66	0.57	4	Dolomite and limestone	Numerical simulation	Liu et al. (2015)
0.7	0.23	4	Limestone and phyllite	Numerical simulation (calibrate)	Zhao et al. (2021)
0.52	0	0.5	Pyroclastic flows	Numerical simulation	Gueugneau et al. (2019)
0.75	0.08	4	Rocks	Numerical simulation (fitted)	Lucas et al. (2014)
0.76	0.15	0.1	Igneous rocks	Laboratory tests (fitted)	Lucas et al. (2014)
0.84	0.11	4.1	Landslides in Hong Kong, Canada, and Mars	Numerical simulation (fitted)	Lucas et al. (2014)

simulation, which were following the recommended values (Liu et al., 2015; Lucas et al., 2014). The internal friction angle (φ) of the sliding mass was determined by the triaxial test. All of the input parameters

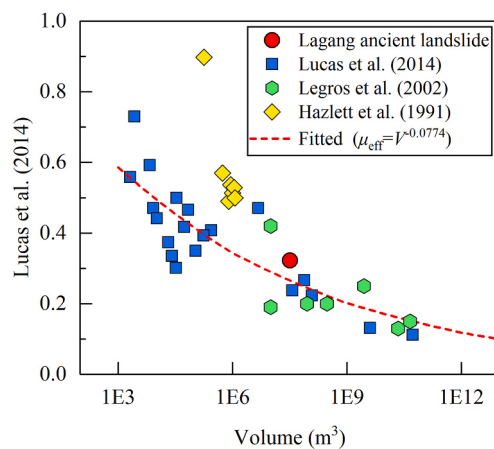


Fig. 6. The volume and friction coefficient of the Lagang ancient landslide, compared with landslides on earth (data from (Hazlett et al., 1991; Legros, 2002; Lucas et al., 2014)).

Table 3
Values for the parametric studies.

Parameters	Values
μ_p	0.4, 0.5, 0.6, 0.7, 0.8
μ_s	0.1, 0.2, 0.3
V_c	1, 5, 10, 15, 20

have been listed in Table 4:

4. Results

4.1. Influenced area and deposits depth

In the first stage, seven sets of numerical tests with different constant friction coefficient ($\mu = 0.3, 0.35, 0.4, 0.45, 0.5, 0.55, 0.6$) were conducted with same initial conditions. The deposition patterns are shown in Fig. 7(a), where the maximum runout distances were labeled. By further extracting the deposition index, it is found that the maximum landslide runout distance (D_{max}) and the friction coefficient μ show a significant negative correlation, which can be expressed as: $D_{max} = -5036.42\mu + 4317.96$ ($R^2 = 0.965$). The above results indicate that the resistance coefficient is one of the key parameters that affect the runout of the landslide, and a small decrease in μ will greatly promote the runout distance of the landslide Fig. 7(b).

Fig. 8a-c shows the accumulation morphology of landslides in three sets of constant friction coefficients ($\mu = 0.4, 0.5, 0.6$). The results indicate that when $\mu = 0.6$, the landslide slides with a maximum runout distance of 1397 m, and the deposits are mainly concentrated at the front of the landslide source area. In contrast, when $\mu = 0.5$ is applied, the runout distance of the landslide is 1773 m, and the influenced range is larger than before. The maximum accumulation thickness is 68 m, and

Table 4
Parameters in the numerical simulation setup.

Parameters	Unit	Value
Density ρ	kg/m³	2700
Internal friction angle φ	°	37
Courant number		5
dx	m	5
dy	m	5
Mesh in X direction		798
Mesh in Y direction		441
Mesh numbers		351,918
Solve time	s	100

the thickness distribution is relatively uniform while the sliding mass in the middle and rear areas are slightly thicker. When $\mu = 0.4$, the runout distance increased to 2187 m, and the maximum accumulation thickness decreased to 63 m.

When fixing the peak friction coefficient and applying the friction weakening model ($\mu_s = 0.3$, $V_c = 4$ m/s), it is found that the maximum runout distance of the sliding mass has reached 2853 m. The front of the sliding mass enters the Yarlung Zangbo River. In three scenarios with resistance weakening, the maximum runout distance of the landslide was increased by 666 m, 1080 m, and 1456 m, respectively, which was almost 130%, 160%, and 204% of the original runout distance. It suggests that the mobility of the landslide is sensitive to the friction coefficient.

The simulation results in Fig. 8d, e, and f also indicate that when using the constant friction coefficient μ_s and critical velocity V_c , both the final runout distance and deposits area of the landslide are almost identical. The reason may be that the low velocity just occurred in the initial stage of the landslide. After that, the velocity quickly reaches and exceeds the velocity threshold due to the high and steep terrain. The friction coefficient of the sliding mass drops to $\mu_s = 0.3$ in a short period, so only small differences in the accumulation form.

4.2. Velocity character

The average velocity is a key indicator of landslide dynamics which reflects its dynamic process. In this study, the average velocity of the sliding mass (V_a) is defined as the ratio of the total momentum of all soil columns to the total volume of the sliding mass in a certain time, which can be expressed as:

$$V_a = \frac{\sum (\sqrt{(hu)^2 + (hv)^2})}{\sum h} \quad (13)$$

The average velocity of the sliding mass in the six scenarios (shown in Fig. 8) was extracted during the simulation. It is found that when the friction weakening is not considered, as the friction coefficient increases from 0.4 to 0.6, the peak of the average velocity of the sliding mass is dropped from 34.8 m/s to 7.8 m/s, almost 77% (Fig. 9). When considering the resistance weakening, the peak average velocity is close to 50 m/s, which is far greater than 20 m/s, the threshold speed of high-speed landslides (Hung et al., 2014; Varnes, 1978). In both three different scenarios (d), (e), and (f), the peak velocity is much larger than the simulation result without considering the weakening of the resistance in the scenarios (a), (b), and (c).

4.3. Friction character

The distribution of the friction coefficient μ at the bottom of the sliding mass in each grid was also monitored at different simulation times. To quantify it, we proposed the average friction coefficient μ_a , which represents the average value of the friction coefficients of all units covered by the sliding mass, and it can be expressed as:

$$\mu_a = \frac{1}{n} \sum_{h>0} \mu_i \quad (14)$$

Where n is the number of unit grids covered by the sliding mass at a specific simulation time.

The result is shown in Fig. 10. As the landslide initialized, the movement velocity of the sliding mass increased rapidly. Since the modeled velocity is generally greater than the velocity threshold of 4 m/s, the average friction coefficient drops rapidly and approaches the stable friction coefficient of 0.3 in the first 5 s. When 40 s elapsed, the average velocity decreases due to the accumulation, and the friction coefficient rises to the initial state. Similar laws are also recorded in the research of Lucas et al. (2014) and An et al. (2021).

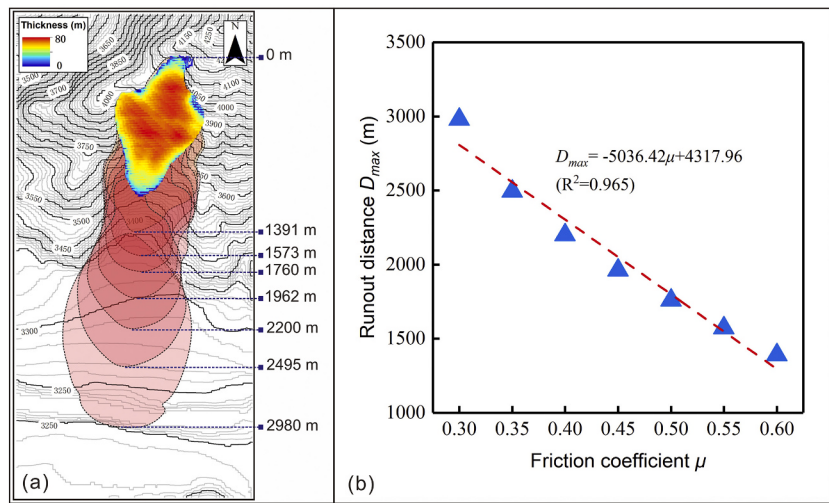


Fig. 7. The maximum runout distance of the landslide with different constant friction coefficients ($\mu = 0.3, 0.35, 0.4, 0.45, 0.5, 0.55, 0.6$). The colored cloud map above the contour lines in Fig. 7(a) represents the initial state before the landslide initial.

A cloud chart of the friction coefficients distribution of scenario (f) is drawn in Fig. 11. The simulation results suggest that in the instability stage ($t = 5$ s), the front and trailing edges of the sliding mass are affected by the locking rock, and the friction coefficients are high for the low-velocity region. In the movement stage ($t = 25$ s), the sliding mass has transformed into a debris avalanche, and the velocity is much greater than the velocity weakening threshold, so it appears as a global weakening. According to the field survey, almost no slippery mass in the source area. When 50 s elapsed, the edges on both left and right sides of the landslide no longer expand, where the high friction. At almost the end of the simulation ($t = 55$ s), the front edge of the sliding mass arrived at the river, while the little sliding mass on the slope accumulates at the toe region, thus showing weakening friction locally. The field observations indicate that there is a large number of loose deposits at the end of the landslide source area (Fig. 3b), which is in agreement with the simulation results. Finally, when the velocity approaches 0 m/s and stops moving, the resistance of covered areas is reached the peak value. As shown in Fig. 11, the varies in the resistance distribution suggest the dynamic process of the Lagang ancient landslide, which also reflects the rationality of the proposed model.

4.4. Dynamic process

The dynamic process of the Lagang ancient landslide is further analyzed based on the simulation results. Taking reference to previous studies (Cui et al., 2019; Guo et al., 2020), a dimensionless parameter Froude number is used, which is defined as:

$$N_{fr} = \frac{v}{\sqrt{gh}} \quad (15)$$

Where v is the landslide velocity, $g = 9.81 \text{ m/s}^2$, is the gravity, and h is the flow depth.

The Froude number N_{fr} represents a ratio of inertial and gravitational forces, which describes different flow regimes of open channel flow. For supercritical flow (fast rapid flow), $N_{fr} > 1$, and $N_{fr} < 1$ for a subcritical flow (slow/tranquil flow). When $N_{fr} = 1$, it represents a critical flow.

Fig. 12(a) shows the variety of N_{fr} over time at the feature points in different regions (P1: source area, P2: transport area, and P3: deposition area) as shown in Fig. 3b. It is noticed that N_{fr} in the source area (P1) quickly rose to 5 and reached the peak within 20 s, and then quickly dropped to below 1, which means that the first wave of fast rapid landslide flow is about 24 s, during which the inertial force was dominant. When 60 passed, N_{fr} rose to about 1, indicating that the residual material in the source area appeared a tranquil flow dominated by

gravity. The N_{fr} in both the transport and deposition area has an upward and downward trend over time, which means the landslide is dominated by the inertial force when passing the P2 and P3. The P2 is located at the toe of the slope, where the deposition thickness is large and the velocity is attenuated, resulting in the peak value of N_{fr} at P2 being smaller than P3.

In Fig. 12(b), the N_{fr} at different simulation moments was extracted to discuss its spatial characteristics. When $t = 0$ s, N_{fr} is occurred in the source area with a value of about 1, indicating a critical flow dominated by gravity here. When $t = 30$ s, the landslide has moved to a horizontal distance of 1200 m. Due to the huge velocity and shallow flow depth at the front of the landslide, N_{fr} is close to 20, indicating that the movement in this area is dominated by inertial force. A similar phenomenon also appeared at the tail of the landslide, which was mainly affected by the slope of the terrain. With the movement of the landslide, the landslide moves to around 1500 m when $t = 50$ s, the N_{fr} still retains the trend of decreasing at both ends to the middle. However, due to the decrease in the landslide speed, the peak value is only half of before. When $t = 70$ s, the landslide is almost stagnant. At this time, N_{fr} is between 0 and 1, with only slight fluctuations, which may be local motion caused by gravity.

4.5. Parametric study

To quantify the sensitivity of the landslide dynamic process to the parameters of the friction weakening model, the results of 75 sets of numerical experiments (shown in Table 3) were recorded. For each scenario, four significant parameters, including maximum runout distance, the maximum widening distance, the influenced region, and the peak velocity were acquired.

Fig. 13a shows the variation of the peak average velocity V_a with the peak friction coefficient μ_p and the critical velocity V_c . The results suggest that when the μ_s is constant, V_a was generally decreasing with the μ_p increases. When the critical velocity is constant, V_a decreases as μ_p increases from 0.4 to 0.7. When μ_p rises to 0.8 and $V_c > 10 \text{ m/s}$, V_a significantly decreases by about 80%. As the μ_s increase to 0.2 and 0.3 (Fig. 13b and c), a similar trend is still established. However, due to the increase of μ_s , V_a generally decreases, and as the V_c and the μ_p increase, the peak velocity decreases significantly more than before.

Fig. 13d-e and g-i show the farthest runout distance and widening of the landslide deposits respectively. When the $\mu_s = 0.1$, the velocity of the sliding mass rapidly rises after the initial and exceeds the velocity threshold, the max runout distance is about 3520 m on the opposite river bank and the maximum width is between 1500 and 1900 m, mainly located in the Yarlung Zangbo River. When the μ_p rises to 0.8 and the V_c

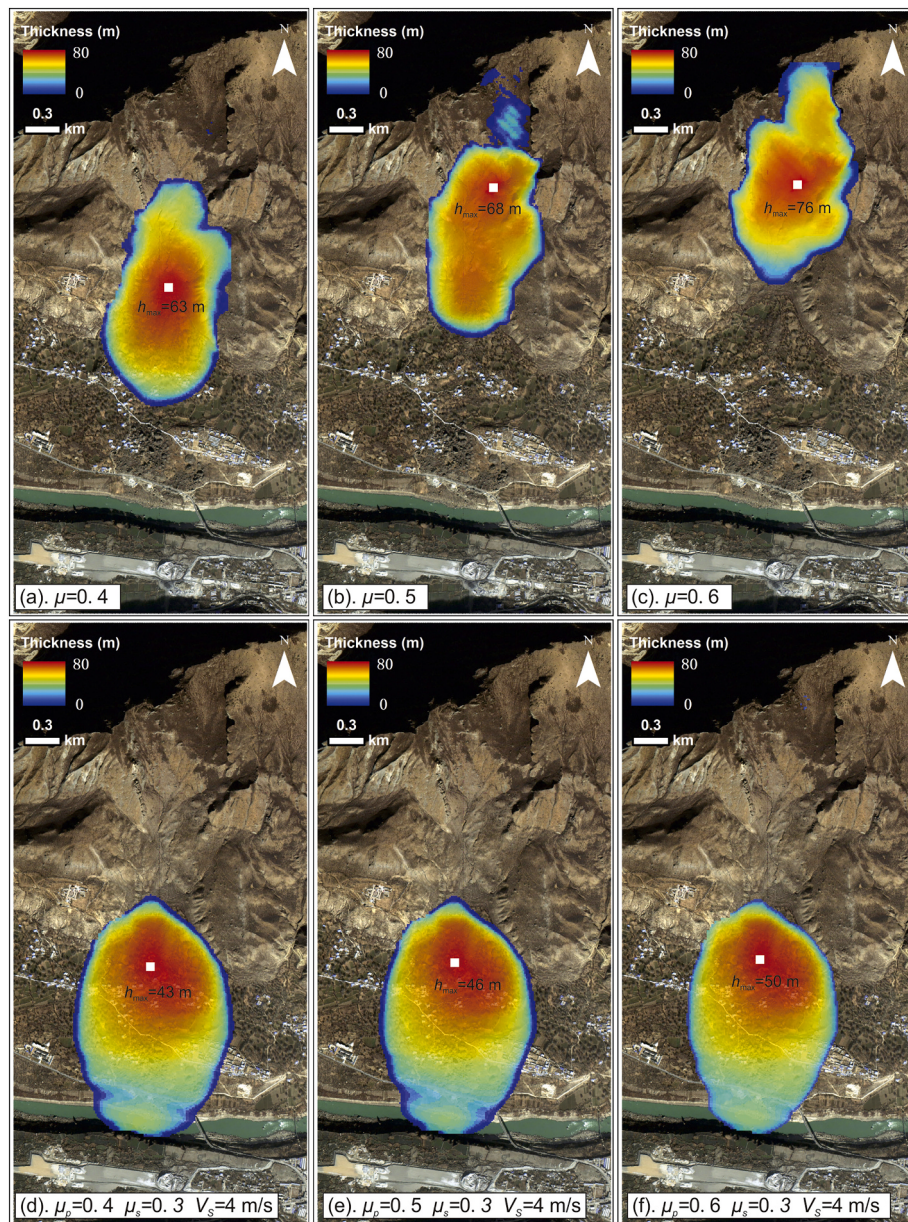


Fig. 8. Simulation results of the Lagang ancient landslide between constant and variety friction coefficient. The constant friction coefficients (0.4, 0.5, and 0.6) were used in (a)-(c), and the same velocity weakening threshold (4 m/s) and steady friction coefficient (0.3) were used in (d)-(f).

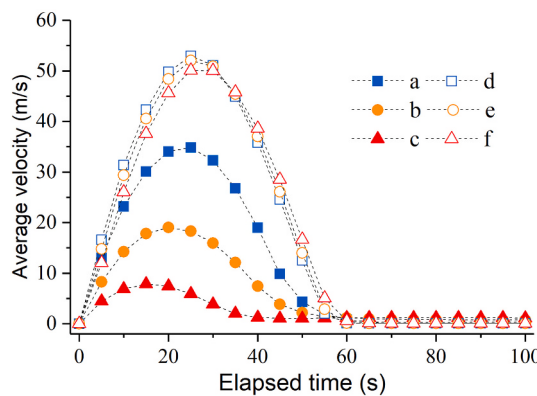


Fig. 9. Varieties of the landslide average velocity (V_a) in the six scenarios with the simulation time.

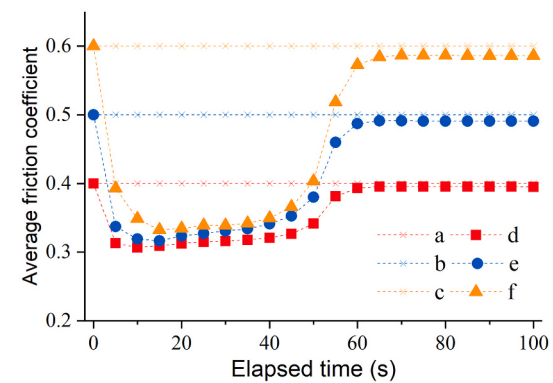


Fig. 10. The variety of the average friction coefficient μ_a in the six simulation scenarios in Fig. 8.

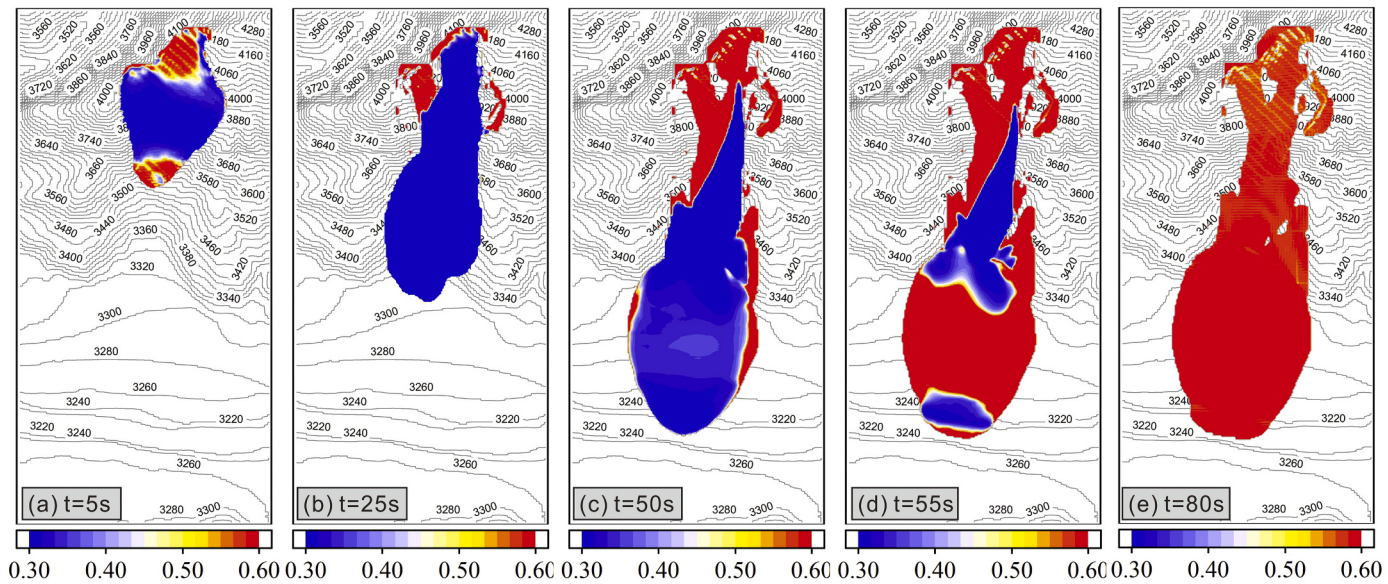


Fig. 11. The distribution of friction coefficients in simulation region over simulation time in simulation scenario (f) ($\mu_s = 0.3$, $\mu_p = 0.6$, $V_c = 4 \text{ m/s}$).

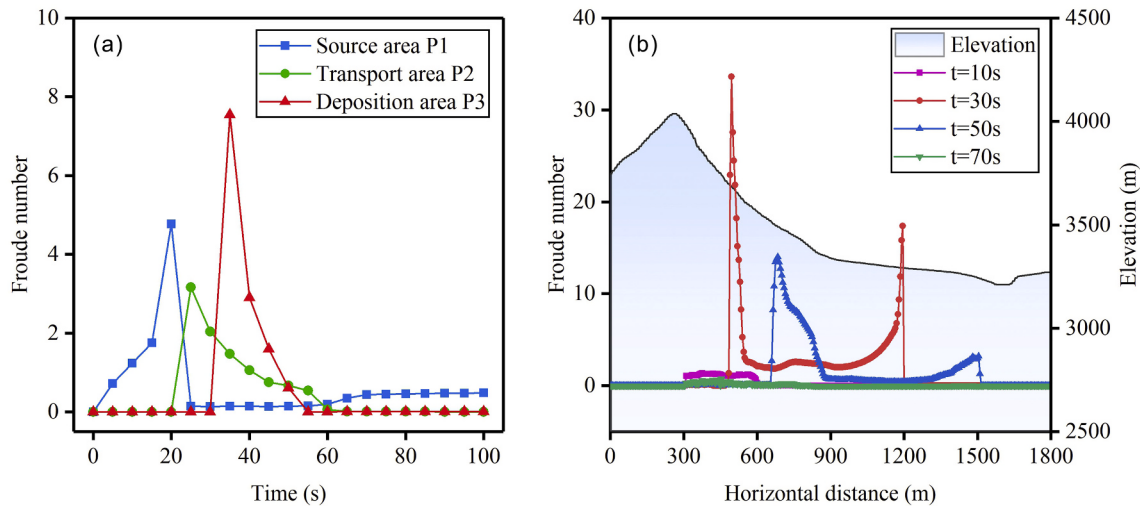


Fig. 12. Variation of the Froude number in different areas of Lagang ancient landslide with (a) simulation time and (b) space position.

exceeds 15 m/s, the velocity was significantly limited, which is less than the threshold velocity, so the maximum runout distance and broadening are reduced. In general, as μ_s increase, the mobility of the landslide is restricted, and both the runout distance and widening are restricted and reduced. Therefore, the landslide-influenced area is also reduced (Fig. 13j-l).

Based on the above results, three-dimensional scatters were drawn in Fig. 14. The color of each scatter point represents the value of (a) peak velocity (b) maximum movement distance (c) maximum widening distance and (d) cover area. It can be found that the steady friction coefficient μ_s has the greatest influence on the landslide dynamic because it determines the lower limit of the friction coefficient of the landslide. The peak friction coefficient μ_p has a relatively small influence on the landslide runout, which is mainly impacting the initial stage of the landslide. The critical velocity V_c is the most critical parameter of the model which determines whether the friction weakening occurs. When V_c is set to a smaller value, the landslide can quickly reach the threshold velocity after starting, and the movement process has a less correlation with the peak friction coefficient μ_p . When V_c takes a large value, it is difficult for the landslide velocity to reach this threshold, so mobility

will be limited.

5. Discussion

5.1. Physical meanings of the parameters

The schematic of the friction weakening model was shown in Fig. 15. Fig. 15(a) shows that in an experiment, the friction coefficient first increased to the peak value with the increase of the shear distance, and finally decreased significantly and stabilized. Because it is almost difficult to continuously change the shear rate in a variety range in an experiment, Fig. 15(b) is a curve statistical law of the resistance change under different shear rates. The results from a series of simulations indicate that three key factors (μ_p , μ_s , and V_c) in the friction weakening model significantly influence the landslide dynamics and deposits. Their physical meaning will be discussed in the following.

The peak friction coefficient (μ_p) represents the stable value of the friction coefficient of the sliding mass in the low-velocity shear. It is affected by the roughness of the internal structural surface of the rock mass or the ground surface. The value is lower for the smooth shear

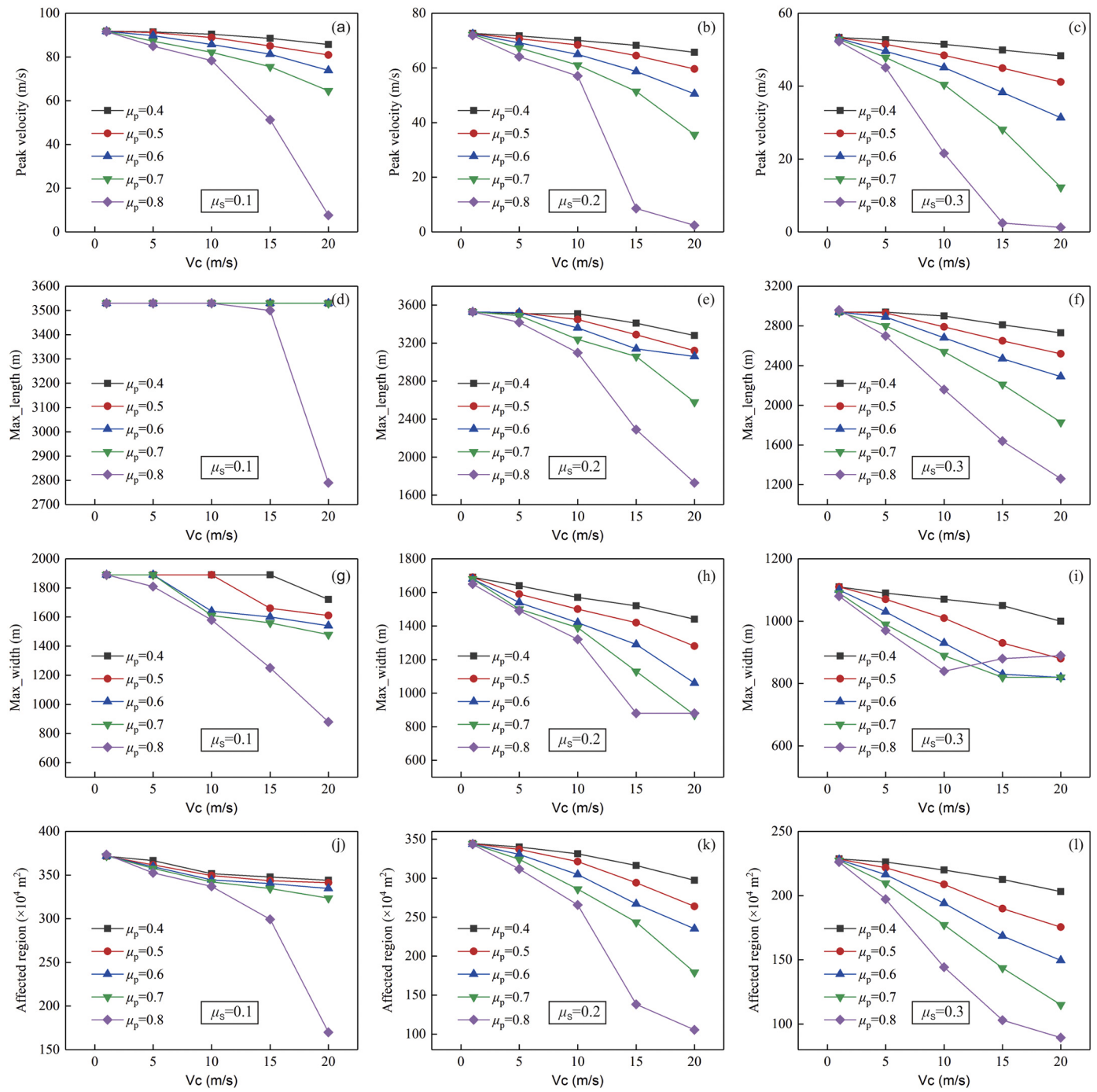


Fig. 13. Statistics of the results of 75 sets of numerical experiments. The figures show the variety of (1) peak velocity (Fig. 13a~13c) (2) maximum runout distance (Fig. 13d~13f) (3) maximum widening distance (Fig. 13g~13i) and (4) influenced regions (Fig. 13j~13l) with different average velocity V_a , peak friction coefficient μ_p and the critical velocity V_c .

structural surface inside the rock mass; conversely, it is higher for the tensile rough structural surface formed by earthquakes and other activations. In addition, factors such as lithology and water content will also affect its value (Ferdousi and Rubin, 2020; Miyamoto et al., 2009).

The steady friction coefficient (μ_s) represents the lower friction coefficient of the sliding mass in high-velocity shearing and is a manifestation of the friction weakening. Both flash heating and particle breakage have been used to explain this phenomenon. Flash heating refers to the liquid or gas generated by minerals melting under the extremely high pressure in sliding mass, which plays a lubricating effect on the sliding mass (Deng et al., 2020; Di Toro et al., 2011). A large

number of studies also indicate that small particle size particles, rather than large blocks, may promote the mobility of the debris avalanche. In other words, the inevitable breakage of the sliding mass may decrease the resistance of the landslide and increase the runout distance (Li et al., 2021a; Lin et al., 2020). This phenomenon may be related to the transmission of the force chain in the landslides, in which the force chain between the coarse skeletons may be dissipated by fine particles wrapped around them (Hu et al., 2021). In all, the steady friction coefficient is related to the conditions of lithology, weathering, and the joint surface that determine its disintegration ability on the one hand, and on the other hand, it is related to external conditions such as normal stress,

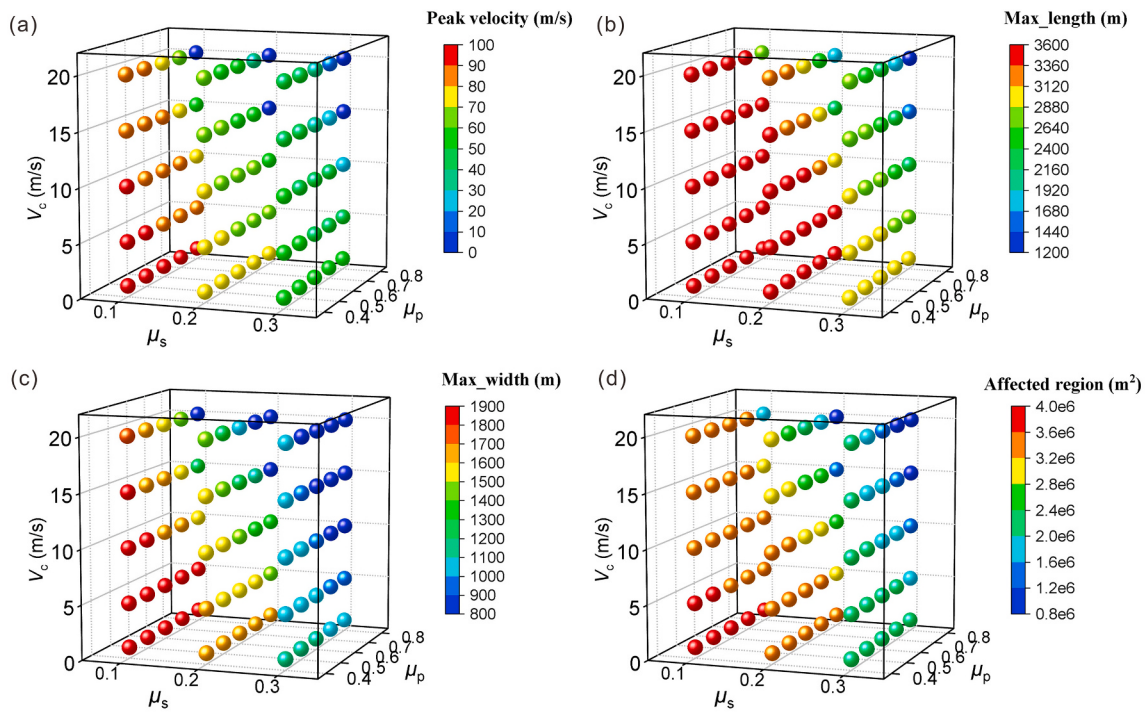


Fig. 14. 3D scatters of the 1) peak velocity 2) maximum runout distance 3) maximum widening distance and 4) influenced region response to parameters μ_p , μ_s , and V_c .

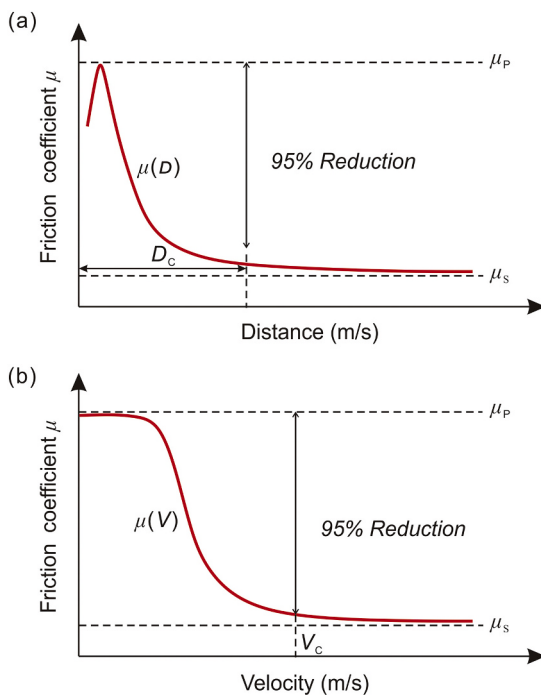


Fig. 15. Schematic diagram of friction weakening model caused by (a) shearing distance increase and (b) shearing velocity variety. (based on Yang et al. (2014)).

shear distance, and velocity. This value is the reflection of the physical properties of the landslide materials.

The critical threshold for the friction weakening of landslide can be divided into two categories, as is shown in Fig. 15, namely the velocity V_c (Togo et al., 2014) used in this article and the distance threshold D_c (Mizoguchi et al., 2007), which can be expressed as:

$$\mu = \mu_s + (\mu_p - \mu_s) e^{ln(0.05)d/D_c} \quad (16)$$

where d is the shearing distance, and D_c represents the shearing distance when the peak friction coefficient drops by 95%.

Both V_c and D_c can be obtained from high-velocity Rotary-shear tests (Table 2). Yang et al. (2014) conducted Rotary-shear experiments with samples of the Taoling landslide and found that the critical threshold D_c ranged from 3 to 8 m, while the V_c was close to 0.15 m/s. The distance threshold seems to be correlated with shear velocity. Other researchers suggest that the critical thresholds may also affect by materials (Jiang et al., 2016) and water content (Miyamoto et al., 2009). The distance threshold is obtained at a specific velocity, therefore, it is not suitable for the landslide dynamic analysis due to the velocity distribution of the sliding mass being different everywhere.

Experimental research on the velocity threshold is always limited by the maximum load normal stress (2 MPa) and shear velocity (2 m/s) (Hu et al., 2020; Igwe et al., 2013; Jiang et al., 2016; Zhang et al., 2011), which is almost impossible to reproduce the stress and the velocity of giant landslides along the Sichuan-Tibet Railway. For instance, the maximum normal stress of the Lagang ancient landslide was estimated to be more than 2.7 MPa and its velocity can reach almost 50 m/s, which is much greater than the maximum loading rate of the instrument. It is also found that with the change of shear velocity and normal pressure, the internal resistance of the sliding mass may show different trends from that in low-velocity shear (Hu et al., 2020). For this reason, it is necessary to carry out a parameter sensitivity analysis on the velocity threshold under the premise of insufficient understanding of the friction weakening mechanisms in high-velocity and long-runout landslides.

5.2. Geological impacts on the model parameters

The formation of the high-velocity and long-runout landslides are significantly related to the evolution of long-term geology, landforms, climate, and other disaster-generating environments (Feng et al., 2021; Ouimet et al., 2007). Therefore, the differences in geological conditions should be taken into account when using the friction weakening model.

Limited by the research on the physical mechanism of the resistance weakening, parameter adjustment was always required to ensure the consistency between the simulation results and the actual accumulations, which has brought great challenges to pre-landslide risk assessment. Here, we give the basic principles of parameter calibration, which may provide references for practice.

When calibrating model parameters, both three main factors need to be considered: altitude, lithology, and rock integrity. The altitude represents the temperature environment in which the landslide develops, the landslides along the Sichuan-Tibet Railway are always located in extremely high-altitude glacier areas (such as the Jiaobunong landslides (Wang et al., 2019a) and Luanshobao landslides (Guo et al., 2016). Both ice splitting, freezing and thawing, and weathering may produce large-scale fissures, which may provide excellent space for melting ice and snow. The coupling of the remaining weathering material and rainfall on the slope will also greatly change the hydrological process in the area, and then induce landslides (Lei et al., 2021; Sun et al., 2021; Zhang et al., 2021b; Zhang et al., 2019). It is reasonable to induce that, the rock mass will start and move with plenty of ice, snow, and water once the landslide occurred, which will significantly reduce its friction (Evans et al., 2009; Shugar et al., 2021; Wang et al., 2019b). So, a relatively small value of μ_s should be used. In addition, the rock mass in a high position was always strong weathering with low integrity. It can be disintegrated at a small shear rate and resulting in weakened resistance. Therefore, a relatively small value of V_c , and μ_f should be applied.

The lithology represents the strength of the sliding mass. Soft rock is difficult to store large elastic strain energy, and small-scaled landslides are usually developed here (Guo et al., 2021). On the contrary, hard rock is easy form giant landslides (Guo et al., 2022; Li et al., 2017; Park and Michalowski, 2017). Hard rock masses have a high peak friction coefficient, and can not be broken and disintegrated without high speeds. Therefore, relevant larger values of V_c and μ_f should be applied. Given the same μ_s in the two types of rocks, the μ_p in the hard rock is larger than that of the soft rock. There is more potential for friction weakening, which may lead to an obvious promotion of landslide runout (see the comparison in Fig. 8a, d, and Fig. 8c, f). Therefore, unexpected huge landslide disasters usually occur in these regions.

As mentioned before, the integrity of the rock mass represents the potential for the fragmentation of the sliding mass. The Tibet Plateau is one of the most active regions of plate tectonics on the earth, where the rock mass is seriously damaged (Yi et al., 2021). Both the macroscopic structure of the rock mass and the microscopic fissures inside the rock are well developed. These fissures may provide a potential structural surface and promote the disintegration and fragmentation of the sliding mass. Therefore, a relatively higher V_c and μ_f should be used for relatively complete rock masses.

It should be noted that the above discussion follows the hypothesis that resistance weakening is dominated by fragmentation. As introduced before, there are a large number of theories that explain the phenomenon of resistance weakening from other perspectives. Since the physical mechanism has not been fully understood, the above results may have limitations. Therefore, relevant experiments need to be explored in both physical and numerical experiments to provide a more accurate reference value for practice.

6. Conclusion

This study establishes a landslide dynamic model for the landslides runout analysis by considering the velocity-based friction weakening model. The Lagang ancient landslide, 500 m from the Jiacha Station, was selected as an example to examine the proposed model and explore the geophysical meaning and influence of the key parameters in the friction weakening model on the landslide dynamics.

The results from 75 numerical tests indicate that the steady friction coefficient (μ_s) determines the lower limit of the friction coefficient, which has the greatest impact on the landslide movement; the peak

average velocity (μ_p) is mainly acted in the initial and deposit stage and has relatively little influence on the landslide dynamic. The critical velocity (V_c) is the most critical parameter of the model. When the V_c is small, the landslide can quickly reach the threshold velocity after starting, and the movement process has a small correlation with μ_p ; when the V_c is large, the landslide is difficult to reach the threshold value, and the landslide mobility will be limited.

The materials, lithology, strength, and the internal micro-cracks of the landslide mass show unique characteristics due to the complex action of the geological, geomorphic, and climatic along the Sichuan-Tibet Railway. These factors may be the internal causes of the ultra-long-distance movement of the landslide. Three indexes (including altitude, lithology, and rock integrity) should be considered to determine the model parameters when conducting landslides risk assessment in this region.

CRediT authorship contribution statement

Jian Guo: Conceptualization, Methodology, Software, Formal analysis, Investigation, Writing – original draft, Funding acquisition. **Yifei Cui:** Methodology, Formal analysis, Writing – original draft, Funding acquisition. **Wenjie Xu:** Software, Formal analysis, Data curation, Writing – original draft. **Wei Shen:** Software, Conceptualization, Writing – original draft. **Tonglu Li:** Methodology, Software, Data curation, Writing – original draft. **Shujian Yi:** Investigation, Data curation, Writing – original draft.

Declaration of Competing Interest

The authors declare that they have no known competing financial interests or personal relationships that could have appeared to influence the work reported in this paper.

Acknowledgments

This study was funded by the National Natural Science Foundation of China (No. 42120104002, 41941019, 42077238, 41941017), the Research Fund Program of the State Key Laboratory of Hydroscience and Engineering (No. 2020-KY-04), the Second Tibetan Plateau Scientific Expedition and Research Program (STEP) (No. 2019QZKK0906), the Key Research Program of Frontier Sciences, CAS (No. QYZDY-SSW-DQC006).

The authors would express our sincere appreciation to anonymous reviewers and editors for their valuable comments and suggestions. The authors would like to thank Prof. Yusheng Li from Chengdu University of Technology, and Shunyu Yao, Hao Wang, Jiao Wang, Guotao Zhang, Chunhao Wu, and Yang Yang from the Institute of Mountain Hazards and Environment, CAS for their assistance in the field investigation and valuable suggestion and discussion.

References

- An, H.C., Ouyang, C.J., Zhou, S., 2021. Dynamic process analysis of the Baige landslide by the combination of DEM and long-period seismic waves. *Landslides* 18, 1625–1639. <https://doi.org/10.1007/s10346-020-01595-0>.
- Bazai, N.A., Cui, P., Carling, P.A., et al., 2021. Increasing glacial lake outburst flood hazard in response to surge glaciers in the Karakoram. *Earth Sci. Rev.* 212, 103432. <https://doi.org/10.1016/j.earscirev.2020.103432>.
- Borykov, T., Mege, D., Mangeney, A., et al., 2019. Empirical investigation of friction weakening of terrestrial and Martian landslides using discrete element models. *Landslides* 16, 1121–1140. <https://doi.org/10.1007/s10346-019-01140-8>.
- Cheng, G., Wu, T., 2007. Responses of permafrost to climate change and their environmental significance, Qinghai-Tibet Plateau. *J. Geophys. Res. Earth Surf.* 112. <https://doi.org/10.1029/2006jf000631>.
- Crespo, A.J.C., Dominguez, J.M., Rogers, B.D., et al., 2015. DualSPHysics: Open-source parallel CFD solver based on Smoothed Particle Hydrodynamics (SPH). *Comput. Phys. Commun.* 187, 204–216. <https://doi.org/10.1016/j.cpc.2014.10.004>.
- Cui, P., Guo, J., 2021. Evolution models, risk prevention and control countermeasures of the valley disaster Chain. *Adv. Eng. Sci.* 53, 5–18. <https://doi.org/10.15961/j.jsusec.202100285>.

- Cui, P., Jia, Y., 2015. Mountain hazards in the Tibetan Plateau: research status and prospects. *Natl. Sci. Rev.* 2, 397–399. <https://doi.org/10.1093/nsr/nwv061>.
- Cui, P., Dang, C., Cheng, Z.L., et al., 2010. Debris flows resulting from Glacial-Lake outburst floods in Tibet, China. *Phys. Geogr.* 31, 508–527. <https://doi.org/10.2747/0272-3646.31.6.508>.
- Cui, S.H., Pei, X.J., Huang, R.Q., 2018. Effects of geological and tectonic characteristics on the earthquake-triggered Daguanbao landslide, China. *Landslides* 15, 649–667. <https://doi.org/10.1007/s10346-017-0899-3>.
- Cui, Y.F., Jiang, Y., Guo, C.X., 2019. Investigation of the initiation of shallow failure in widely graded loose soil slopes considering interstitial flow and surface runoff. *Landslides* 16, 815–828. <https://doi.org/10.1007/s10346-018-01129-9>.
- Cui, P., Peng, J., Shi, P., et al., 2021. Scientific challenges of research on natural hazard and disaster risk. *Geogr. Sustain.* <https://doi.org/10.1016/j.geosus.2021.09.001>.
- Cundall, P.A., Strack, O.D.L., 1979. A discrete numerical model for granular assemblies. *Geotechnique* 29, 47–65. <https://doi.org/10.1680/geot.1979.29.1.47>.
- Dai, F.C., Lee, C.F., Ngai, Y.Y., 2002. Landslide risk assessment and management: an overview. *Eng. Geol.* 64, 65–87. [https://doi.org/10.1016/S0013-7952\(01\)00093-X](https://doi.org/10.1016/S0013-7952(01)00093-X).
- Dai, Z., Wang, F., Cheng, Q., et al., 2019. A giant historical landslide on the eastern margin of the Tibetan Plateau. *Bull. Eng. Geol. Environ.* 78, 2055–2068. <https://doi.org/10.1007/s10064-017-1226-x>.
- Deng, Y., He, S., Scaringi, G., et al., 2020. Mineralogical analysis of selective melting in partially coherent rocksides: bridging solid and molten friction. *J. Geophys. Res. Solid Earth* 125. <https://doi.org/10.1029/2020jb019453>.
- Deng, J., Gao, Y., Yao, X., et al., 2021. Recognition and implication of basu giant rock avalanche. *Adv. Eng. Sci.* 53, 19–28. <https://doi.org/10.15961/j.jseue.202100319>.
- Dergachev, V.A., 2015. Length of the current interglacial period and interglacial intervals of the last million years. *Geomagn. Aeron.* 55, 945–952. <https://doi.org/10.1134/s0016793215070051>.
- Di Toro, G., Han, R., Hirose, T., et al., 2011. Fault lubrication during earthquakes. *Nature* 471, 494–498. <https://doi.org/10.1038/nature09838>.
- Diao, Y., Espinosa-Marzal, R.M., 2018. The role of water in fault lubrication. *Nat. Commun.* 9, 2309. <https://doi.org/10.1038/s41467-018-04782-9>.
- Dong, J.J., Yang, C.M., Yu, W.L., et al., 2013. Velocity-displacement dependent friction coefficient and the kinematics of giant landslide. *Earthquake-Induced Landslides* 395–401. https://doi.org/10.1007/978-3-642-32238-9_41.
- Evans, S.G., Tutubalina, O.V., Drobyshev, V.N., et al., 2009. Catastrophic detachment and high-velocity long-runout flow of Kolkta Glacier, Caucasus Mountains, Russia in 2002. *Geomorphology* 105, 314–321. <https://doi.org/10.1016/j.geomorph.2008.10.008>.
- Fan, X., Yang, F., Siva Subramanian, S., et al., 2019a. Prediction of a multi-hazard chain by an integrated numerical simulation approach: the Baige landslide, Jinsha River, China. *Landslides* 17, 147–164. <https://doi.org/10.1007/s10346-019-01313-5>.
- Fan, X.M., Scaringi, G., Korup, O., et al., 2019b. Earthquake-induced chains of geologic hazards: patterns, mechanisms, and impacts. *Rev. Geophys.* 57, 421–503. <https://doi.org/10.1029/2018rg000626>.
- Feng, L., Zhang, S., Jin, Z., et al., 2021. The critical mechanics of the initiation of loess flow failure and implications for landslides. *Eng. Geol.* 288 <https://doi.org/10.1016/j.enggeo.2021.106165>.
- Ferdowsi, B., Rubin, A.M., 2020. A granular physics-based view of fault friction experiments. *J. Geophys. Res. Solid Earth* 125. <https://doi.org/10.1029/2019jb019016>.
- Frank, F., McArdell, B.W., Huggel, C., et al., 2015. The importance of entrainment and bulking on debris flow runout modeling: examples from the Swiss Alps. *Nat. Hazards Earth Syst. Sci.* 15, 2569–2583. <https://doi.org/10.5194/nhess-15-2569-2015>.
- Goren, L., Aharonov, E., 2007. Long runout landslides: the role of frictional heating and hydraulic diffusivity. *Geophys. Res. Lett.* 34 <https://doi.org/10.1029/2006gl028895>.
- Gueugneau, V., Kelfoun, K., Druitt, T., 2019. Investigation of surge-derived pyroclastic flow formation by numerical modelling of the 25 June 1997 dome collapse at Soufrière Hills Volcano, Montserrat. *Bull. Volcanol.* 81 <https://doi.org/10.1007/s00445-019-1284-y>.
- Guo, C., Zhang, Y., Montgomery, D.R., et al., 2016. How unusual is the long-runout of the earthquake-triggered giant Luanshibao landslide, Tibetan Plateau, China? *Geomorphology* 259, 145–154. <https://doi.org/10.1016/j.geomorph.2016.02.013>.
- Guo, J., Yi, S.J., Yin, Y.Z., et al., 2020. The effect of topography on landslide kinematics: a case study of the Jichang town landslide in Guizhou, China. *Landslides* 17, 959–973. <https://doi.org/10.1007/s10346-019-01339-9>.
- Guo, J., Wang, J., Li, Y., et al., 2021. Discussions on the transformation conditions of Wangcang landslide-induced debris flow. *Landslides* 18, 1833–1843. <https://doi.org/10.1007/s10346-021-01650-4>.
- Guo, J., Cui, Y.F., Xu, W.J., et al., 2022. Numerical investigation of the landslide-debris flow transformation process considering topographic and entrainment effects: a case study. *Landslides* 19, 773–788. <https://doi.org/10.1007/s10346-021-01791-6>.
- Hazzlett, R.W., Buesch, D., Anderson, J.L., et al., 1991. Geology, failure conditions, and implications of seismogenic avalanches of the 1944 eruption at Vesuvius, Italy. *J. Volcanol. Geotherm. Res.* 47, 249–264.
- Hu, W., Chang, C.S., McSaveney, M., et al., 2020. A weakening rheology of dry granular flows with extensive brittle grain damage in high-speed rotary shear experiments. *Geophys. Res. Lett.* 47 <https://doi.org/10.1029/2020GL087763>.
- Hu, Y.-X., Li, H.-B., Lu, G.-D., et al., 2021. Influence of size gradation on particle separation and the motion behaviors of debris avalanches. *Landslides*. <https://doi.org/10.1007/s10346-020-01596-z>.
- Hungr, O., Leroueil, S., Picarelli, L., 2014. The Varnes classification of landslide types, an update. *Landslides* 11, 167–194. <https://doi.org/10.1007/s10346-013-0436-y>.
- Hussin, H.Y., Luna, B.Q., van Westen, C.J., et al., 2012. Parameterization of a numerical 2-D debris flow model with entrainment: a case study of the Faucon catchment, Southern French Alps. *Nat. Hazards Earth Syst. Sci.* 12, 3075–3090. <https://doi.org/10.5194/nhess-12-3075-2012>.
- Igwe, O., Wang, F., Sassa, K., et al., 2013. The laboratory evidence of phase transformation from landslide to debris flow. *Geosci. J.* 18, 31–44. <https://doi.org/10.1007/s12303-013-0049-4>.
- Iverson, R.M., 2012. Elementary theory of bed-sediment entrainment by debris flows and avalanches. *J. Geophys. Res. Earth Surf.* 117, n/a-n/a. <https://doi.org/10.1029/2011jf002189>.
- Jiang, Y., Wang, G., Kamai, T., 2016. Fast shear behavior of granular materials in ring-shear tests and implications for rapid landslides. *Acta Geotech.* 12, 645–655. <https://doi.org/10.1007/s11440-016-0508-y>.
- Kang, C., Chan, D., 2018. A progressive entrainment runout model for debris flow analysis and check for its application. *Geomorphology* 323, 25–40. <https://doi.org/10.1016/j.geomorph.2018.09.003>.
- Kuwano, O., Hatano, T., 2011. Flash weakening is limited by granular dynamics. *Geophys. Res. Lett.* 38, n/a-n/a. <https://doi.org/10.1029/2011gl048530>.
- Legros, F., 2002. The mobility of long-runout landslides. *Eng. Geol.* 63, 301–331. [https://doi.org/10.1016/S0013-7952\(01\)00090-4](https://doi.org/10.1016/S0013-7952(01)00090-4).
- Lei, M., Cui, Y., Ni, J., et al., 2021. Temporal evolution of the hydromechanical properties of soil-root systems in a forest fire in China. *Sci. Total Environ.* 151165 <https://doi.org/10.1016/j.scitotenv.2021.151165>.
- Li, C.D., Wang, X.Y., Tang, H.M., et al., 2017. A preliminary study on the location of the stabilizing piles for colluvial landslides with interbedding hard and soft bedrocks. *Eng. Geol.* 224, 15–28. <https://doi.org/10.1016/j.enggeo.2017.04.020>.
- Li, J., Chen, N.S., Zhao, Y.D., et al., 2020a. A catastrophic landslide triggered debris flow in China's Yigong: factors, dynamic processes, and tendency. *Earth Sci. Res. J.* 24, 71–82. <https://doi.org/10.1544/esrj.v24n1.78094>.
- Li, Y., Chen, J., Zhou, F., et al., 2020b. Identification of ancient river-blocking events and analysis of the mechanisms for the formation of landslide dams in the Suwalong section of the upper Jinsha River, SE Tibetan Plateau. *Geomorphology* 368, 107351. <https://doi.org/10.1016/j.geomorph.2020.107351>.
- Li, K., Wang, Y.F., Lin, Q.W., et al., 2021a. Experiments on granular flow behavior and deposit characteristics: implications for rock avalanche kinematics. *Landslides* 18, 1779–1799. <https://doi.org/10.1007/s10346-020-01607-z>.
- Li, Y., Cui, P., Ye, C.M., et al., 2021b. Accurate prediction of earthquake-induced landslides based on deep learning considering landslide source area. *Remote Sens.* 13 <https://doi.org/10.3390/rs13173436>.
- Liang, D., Falconer, R.A., Lin, B., 2006. Comparison between TVD-MacCormack and ADI-type solvers of the shallow water equations. *Adv. Water Resour.* 29, 1833–1845. <https://doi.org/10.1016/j.advwatres.2006.01.005>.
- Lin, Q.W., Cheng, Q.G., Li, K., et al., 2020. Contributions of rock mass structure to the emplacement of fragmenting rockfalls and rockslides: insights from laboratory experiments. *J. Geophys. Res. Solid Earth* 125. <https://doi.org/10.1029/2019JB019296>.
- Liu, W., He, S., Li, X., et al., 2015. Two-dimensional landslide dynamic simulation based on a velocity-weakening friction law. *Landslides* 13, 957–965. <https://doi.org/10.1007/s10346-015-0632-z>.
- Liu, D.Z., Cui, Y.F., Guo, J., et al., 2020. Investigating the effects of clay/sand content on depositional mechanisms of submarine debris flows through physical and numerical modeling. *Landslides* 17, 1863–1880. <https://doi.org/10.1007/s10346-020-01387-6>.
- Lucas, A., Mangeney, A., Ampuero, J.P., 2014. Frictional velocity-weakening in landslides on Earth and on other planetary bodies. *Nat. Commun.* 5, 3417. <https://doi.org/10.1038/ncomms4417>.
- Midi, G.D.R., 2004. On dense granular flows. *Eur. Phys. J. E Soft Matter.* 14, 341–365. <https://doi.org/10.1140/epje/i2003-10153-0>.
- Mikos, M., Bezak, N., 2021. Debris flow modelling using RAMMS model in the alpine environment with focus on the model parameters and main characteristics. *Front. Earth Sci.* 8 <https://doi.org/10.3389/feart.2020.605061>.
- Miyamoto, Y., Shimamoto, T., Togo, T., et al., 2009. Dynamic weakening of shale and bedding-parallel fault gouge as a possible mechanism for Tsaoeling landslide induced by 1999 Chi-Chi earthquake. In: *The Next Generation of Research on Earthquake-induced Landslides: An International Conference in Commemoration of 10th Anniversary of the Chi-Chi Earthquake*, pp. 398–401.
- Mizoguchi, K., Hirose, T., Shimamoto, T., et al., 2007. Reconstruction of seismic faulting by high-velocity friction experiments: An example of the 1995 Kobe earthquake. *Geophys. Res. Lett.* 34 <https://doi.org/10.1029/2006gl027931>.
- Ouimet, W.B., Whipple, K.X., Royden, L.H., et al., 2007. The influence of large landslides on river incision in a transient landscape: Eastern margin of the Tibetan Plateau (Sichuan, China). *Geol. Soc. Am. Bull.* 119, 1462–1476. <https://doi.org/10.1130/B26136.1>.
- Ouyang, C.J., He, S.M., Xu, Q., et al., 2013. A MacCormack-TVD finite difference method to simulate the mass flow in mountainous terrain with variable computational domain. *Comput. Geosci.* 52, 1–10. <https://doi.org/10.1016/j.cageo.2012.08.024>.
- Ouyang, C.J., Zhao, W., He, S.M., et al., 2017. Numerical modeling and dynamic analysis of the 2017 Xinmo landslide in Maoxian County, China. *J. Mt. Sci.* 14, 1701–1711. <https://doi.org/10.1007/s11629-017-4613-7>.
- Ouyang, C., Wang, Z., An, H., et al., 2019. An example of a hazard and risk assessment for debris flows—a case study of Niwan Gully, Wudu, China. *Eng. Geol.* 263, 105351 <https://doi.org/10.1016/j.enggeo.2019.105351>.
- Pan, G., Wang, L., Li, R., et al., 2012. Tectonic evolution of the Qinghai-Tibet Plateau. *J. Asian Earth Sci.* 53, 3–14. <https://doi.org/10.1016/j.jseaes.2011.12.018>.
- Park, D., Michalowski, R.L., 2017. Three-dimensional stability analysis of slopes in hard soil/soft rock with tensile strength cut-off. *Eng. Geol.* 229, 73–84. <https://doi.org/10.1016/j.enggeo.2017.09.018>.

- Peng, J., Cui, P., Zhuang, J., 2020. Challenges to engineering geology of SichuanTibet railway. *Chin. J. Rock Mech. Eng.* 39, 2377–2389. <https://doi.org/10.13722/j.cnki.jrme.2020.0446>.
- Pudasaini, S.P., Krautblatter, M., 2014. A two-phase mechanical model for rock-ice avalanches. *J. Geophys. Res. Earth Surf.* 119, 2272–2290. <https://doi.org/10.1002/2014jf003183>.
- Qi, T., Meng, X., Qing, F., et al., 2021. Distribution and characteristics of large landslides in a fault zone: a case study of the NE Qinghai-Tibet Plateau. *Geomorphology* 379, 107592. <https://doi.org/10.1016/j.geomorph.2021.107592>.
- Sassa, K., Nagai, O., Solidum, R., et al., 2010. An integrated model simulating the initiation and motion of earthquake and rain induced rapid landslides and its application to the 2006 Leyte landslide. *Landslides* 7, 219–236. <https://doi.org/10.1007/s10346-010-0230-z>.
- Savage, S., Hutter, C., 1989. The motion of a finite mass of granular material down a rough incline. *J. Fluid Mech.* 199, 177–215. <https://doi.org/10.1017/S0022112089000340>.
- Schaub, Y., Hugel, C., Cochachin, A., 2015. Ice-avalanche scenario elaboration and uncertainty propagation in numerical simulation of rock-/ice-avalanche-induced impact waves at Mount Hualcán and Lake 513, Peru. *Landslides* 13, 1445–1459. <https://doi.org/10.1007/s10346-015-0658-2>.
- Shen, W., Li, T.L., Li, P., et al., 2018. A modified finite difference model for the modeling of flowslides. *Landslides* 15, 1577–1593. <https://doi.org/10.1007/s10346-018-0980-6>.
- Shen, W., Li, T.L., Li, P., et al., 2019a. A two-layer numerical model for simulating the frontal plowing phenomenon of flow-like landslides. *Eng. Geol.* 259, 12. <https://doi.org/10.1016/j.enggeo.2019.105168>.
- Shen, W., Li, T.L., Li, P., et al., 2019b. The influence of the bed entrainment-induced rheology and topography changes on the propagation of flow-like landslides: a numerical investigation. *Bull. Eng. Geol. Environ.* 78, 4771–4785. <https://doi.org/10.1007/s10064-018-01447-1>.
- Shen, W., Li, T.-L., Berti, M., et al., 2021. Numerical modeling of bed deposition in rapid flow-like landslides: a case study of the Gaolao landslide in Shaanxi Province, China. *J. Mt. Sci.* <https://doi.org/10.1007/s11629-020-6164-6>.
- Shi, G.H., Goodman, R.E., 2010. Two dimensional discontinuous deformation analysis. *Int. J. Numer. Anal. Methods Geomech.* 9, 541–556. <https://doi.org/10.1002/nag.1610090604>.
- Shugar, D.H., Jacquemart, M., Shean, D., et al., 2021. A massive rock and ice avalanche caused the 2021 disaster at Chamoli, Indian Himalaya. *Science*. <https://doi.org/10.1126/science.abb4455>.
- Stoker, J.J., Lindsay, R.B., 1958. Water waves. *Phys. Today* 11, 28–30. <https://doi.org/10.1063/1.3062689>.
- Sulsky, D., Chen, Z., Schreyer, H.L., 1994. A particle method for history-dependent materials. *Comput. Methods Appl. Mech. Eng.* 118, 179–196. [https://doi.org/10.1016/0045-7825\(94\)00033-6](https://doi.org/10.1016/0045-7825(94)00033-6).
- Sun, X., Zhang, G., Wang, J., et al., 2021. Spatiotemporal variation of flash floods in the Hengduan Mountains region affected by rainfall properties and land use. *Nat. Hazards*. <https://doi.org/10.1007/s11069-021-05061-5>.
- Togo, T., Shimamoto, T., Dong, J.J., et al., 2014. Triggering and runaway processes of catastrophic Tsaojing landslide induced by the 1999 Taiwan Chi-Chi earthquake, as revealed by high-velocity friction experiments. *Geophys. Res. Lett.* 41, 1907–1915. <https://doi.org/10.1002/2013gl059169>.
- Varnes, D., 1978. *Slope Movement Types and Processes*.
- Wang, F.W., Sassa, K., 2010. Landslide simulation by a geotechnical model combined with a model for apparent friction change. *Phys. Chem. Earth* 35, 149–161. <https://doi.org/10.1016/j.pce.2009.07.006>.
- Wang, Y.F., Cheng, Q.G., Lin, Q.W., et al., 2018. Insights into the kinematics and dynamics of the Luanshobao rock avalanche (Tibetan Plateau, China) based on its complex surface landforms. *Geomorphology* 317, 170–183. <https://doi.org/10.1016/j.geomorph.2018.05.025>.
- Wang, H., Cui, P., Liu, D.Z., et al., 2019a. Evolution of a landslide-dammed lake on the southeastern Tibetan Plateau and its influence on river longitudinal profiles. *Geomorphology* 343, 15–32. <https://doi.org/10.1016/j.geomorph.2019.06.023>.
- Wang, W., Yang, J., Wang, Y., 2019b. Dynamic processes of 2018 Sedongpu landslide in Namcha Barwa-Gyalpa Peri massif revealed by broadband seismic records. *Landslides* 17, 409–418. <https://doi.org/10.1007/s10346-019-01315-3>.
- Wei, K., Ouyang, C., Duan, H., et al., 2020. Reflections on the catastrophic 2020 Yangtze River Basin flooding in Southern China. *Innovation* 1, 100038. <https://doi.org/10.1016/j.xinn.2020.100038>.
- Wu, R., Zhang, Y., Guo, C., et al., 2018. Characteristics and formation mechanisms of the Lagangcun giant ancient landslide in Jiacha, Tibet. *Acta Geol. Sin.* <https://doi.org/10.3969/j.issn.0001-5717.2018.06.015>.
- Xue, Y., Kong, F., Li, S., et al., 2021. China starts the world's hardest "Sky-High Road" project: challenges and countermeasures for Sichuan-Tibet railway. *Innovation* 2, 2. <https://doi.org/10.1016/j.xinn.2021.100105>.
- Yan, Y., Cui, Y.F., Guo, J., et al., 2020. Landslide reconstruction using seismic signal characteristics and numerical simulations: Case study of the 2017 "6.24" Xinmo landslide. *Eng. Geol.* 270, 15. <https://doi.org/10.1016/j.enggeo.2020.105582>.
- Yan, Y., Cui, Y., Liu, D., et al., 2021. Seismic signal characteristics and interpretation of the 2020 "6.17" Danbe landslide dam failure hazard chain process. *Landslides* 18, 2175–2192. <https://doi.org/10.1007/s10346-021-01657-x>.
- Yang, C.-M., Yu, W.-L., Dong, J.-J., et al., 2014. Initiation, movement, and run-out of the giant Tsaojing landslide — what can we learn from a simple rigid block model and a velocity-displacement dependent friction law? *Eng. Geol.* 182, 158–181. <https://doi.org/10.1016/j.enggeo.2014.08.008>.
- Yi, S., Cui, P., Wu, C., et al., 2021. Control effects of suture zones on distribution of soft rock and its engineering influence along Sichuan-Tibet railway corridor. *J. Eng. Geol.* 29, 275–288. <https://doi.org/10.13544/j.cnki.jeg.2021-0099>.
- Yin, Y.P., Zheng, W.M., Li, X.C., et al., 2011. Catastrophic landslides associated with the M8.0 Wenchuan earthquake. *Bull. Eng. Geol. Environ.* 70, 15–32. <https://doi.org/10.1007/s10064-010-034-7>.
- Zeng, Q.L., Yuan, G.X., Davies, T., et al., 2020. Be-10 dating and seismic origin of Luanshobao rock avalanche in SE Tibetan Plateau and implications on Litang active fault. *Landslides* 17, 1091–1104. <https://doi.org/10.1007/s10346-019-01319-z>.
- Zhang, M., McSaveney, M.J., 2017. Rock avalanche deposits store quantitative evidence on internal shear during runout. *Geophys. Res. Lett.* 44, 8814–8821. <https://doi.org/10.1002/2017gl073774>.
- Zhang, M., Yin, Y.P., Hu, R.L., et al., 2011. Ring shear test for transform mechanism of slide-debris flow. *Eng. Geol.* 118, 55–62. <https://doi.org/10.1016/j.enggeo.2011.01.006>.
- Zhang, G., Cui, P., Yin, Y., et al., 2019. Real-time monitoring and estimation of the discharge of flash floods in a steep mountain catchment. *Hydrol. Process.* 33, 3195–3212. <https://doi.org/10.1002/hyp.13551>.
- Zhang, G., Cui, P., Gualtieri, C., et al., 2021a. Stormflow generation in a humid forest watershed controlled by antecedent wetness and rainfall amounts. *J. Hydrol.* 603, 127107. <https://doi.org/10.1016/j.jhydrol.2021.127107>.
- Zhang, G., Cui, P., Jin, W., et al., 2021b. Changes in hydrological behaviours triggered by earthquake disturbance in a mountainous watershed. *Sci. Total Environ.* 760, 143349. <https://doi.org/10.1016/j.scitotenv.2020.143349>.
- Zhao, S., He, S., Li, X., et al., 2021. The Xinmo rockslide-debris avalanche: An analysis based on the three-dimensional material point method. *Eng. Geol.* 287. <https://doi.org/10.1016/j.enggeo.2021.106109>.
- Zhou, J.W., Cui, P., Hao, M.H., 2016. Comprehensive analyses of the initiation and entrainment processes of the 2000 Yigong catastrophic landslide in Tibet, China. *Landslides* 13, 39–54. <https://doi.org/10.1007/s10346-014-0553-2>.
- Zhou, L., Liu, W., Chen, X., et al., 2021. Relationship between Dams, Knickpoints and the Longitudinal Profile of the Upper Indus River. *Front. Earth Sci.* 9. <https://doi.org/10.3389/feart.2021.660996>.
- Zhu, L., Pei, X.J., Cui, S.H., et al., 2020. On the initiation mechanism of the Daguangbao landslide triggered by the 2008 Wenchuan (Ms 7.9) earthquake. *Soil Dyn. Earthq. Eng.* 137. <https://doi.org/10.1016/j.soildyn.2020.106272>.
- Zoppou, C., Roberts, S., 2000. Numerical solution of the two-dimensional unsteady dam break. *Appl. Math. Model.* 24, 457–475. [https://doi.org/10.1016/s0307-904x\(99\)00056-6](https://doi.org/10.1016/s0307-904x(99)00056-6).
- Zou, Q., Zhou, G.G.D., Li, S.S., et al., 2017. Dynamic process analysis and hazard prediction of debris flow in eastern Qinghai-Tibet Plateau area-a case study at Ridi Gully. *Arct. Antarct. Alp. Res.* 49, 373–390. <https://doi.org/10.1657/aaar0017-019>.